Obesity causes irreversible mitochondria failure in visceral adipose tissue despite successful anti-obesogenic lifestyle-based interventions

Authors:

Alba Gonzalez-Franquesa*‡[1,2], Pau Gama-Perez‡[1], Marta Kulis[3], Norma Dahdah[1], Sonia Moreno-Gomez[1], Ana Latorre-Pellicer[4,5], Rebeca Fernández-Ruiz[6,7], Antoni Aguilar-Mogas[8], Erika Monelli[9], Sara Samino[7,10], Joan Miró[7,10], Gregor Oemer[11], Xavier Duran[7,12], Estrella Sanchez-Rebordelo[13], Marc Schneeberger[6,14], Merce Obach[6], Joel Montane[6,15], Giancarlo Castellano[3], Vicente Chapaprieta[3], Lourdes Navarro[1], Ignacio Prieto[16] ,Carlos Castaño[6], Anna Novials[6,7], Ramon Gomis[6,7], Maria Monsalve[16], Marc Claret[7,17], Mariona Graupera[9], Guadalupe Soria[18], Joan Vendrell[7,12], Sonia Fernandez-Veledo[7,12], Jose Antonio Enríquez[19], Angel Carracedo[4,20], José Carlos Perales[1,21], Rubén Nogueiras[13,22], Laura Herrero[22,23], Markus A. Keller[11], Oscar Yanes[7,10], Marta Sales-Pardo[8], Roger Guimerà[8,24], José Ignacio Martín-Subero[3,24,25], Pablo M. Garcia-Roves*[1,21]

Affiliations:

[1]Department of Physiological Sciences, Universitat de Barcelona, 08907 Barcelona, Spain. [2]Novo Nordisk Foundation Center for Basic Metabolic Research, University of Copenhagen, Denmark. [3]Biomedical Epigenomics Group, Institut d'Investigacions Biomèdiques August Pi i Sunyer (IDIBAPS), 08036 Barcelona, Spain. [4]Grupo de Medicina Xenómica, CIBERER, Centre for Research in Molecular Medicine and

Chronic Diseases (CIMUS), Universidade de Santiago de Compostela, 15782 Santiago de Compostela, Spain. [5]Unit of Clinical Genetics and Functional Genomics, Department of Pharmacology-Physiology, School of Medicine, University of Zaragoza, CIBERER-GCV02 and ISS-Aragon, 50009 Zaragoza, Spain. [6]Diabetes and Obesity Research Laboratory, Institut d'Investigacions Biomèdiques August Pi i Sunyer (IDIBAPS), 08036 Barcelona, Spain. [7]Centro de Investigación Biomédica en Red Diabetes y Enfermedades Metabólicas Asociadas (CIBERDEM), 28029 Madrid, Spain. [8]Department of Chemical Engineering, Universitat Rovira i Virgili, 43007 Tarragona, Spain. [9]Vascular Signalling Laboratory, Program Against Cancer Therapeutic Resistance (ProCURE), Institut d'Investigació Biomèdica de Bellvitge (IDIBELL), 08907 Barcelona, Spain. [10]Metabolomics Platform, IISPV, Department of Electronic Engineering, Universitat Rovira i Virgili, 43007 Tarragona, Spain. [11]Institute of Human Genetics, Medical University of Innsbruck, 6020 Innsbruck, Austria. [12]Institut d'Investigació Sanitària Pere Virgili (IISPV), 43204 Reus, Spain. [13]Department of Physiology, CIMUS, Universidad de Santiago de Compostela, 15782 Santiago de Compostela, Spain. [14]Laboratory of Molecular Genetics, Howard Hughes Medical Institute, The Rockefeller University, NY10065 New York, USA. [15]Blanquerna School of Health Science, Ramon Llull University, Barcelona, Spain. [16]Instituto de Investigaciones Biomédicas Alberto Sols (CSIC-UAM), 28029 Madrid, Spain. [17]Neuronal Control of Metabolism Laboratory, Institut d'Investigacions Biomèdiques August Pi i Sunyer (IDIBAPS), 08036 Barcelona, Spain. [18]Experimental 7T MRI Unit, Institut d'Investigacions Biomèdiques August Pi i Sunyer (IDIBAPS), Barcelona, Spain. [19]Centro Nacional de Investigaciones Cardiovasculares Carlos III, Madrid, Spain; CIBERFES, 28029 Madrid, Spain.

[20]Fundación Pública Galega de Medicina Xenómica, SERGAS, Instituto de Investigación Sanitaria de Santiago de Compostela (IDIS), Santiago de Compostela, Spain. [21]Nutrition, Metabolism and Gene therapy Group; Diabetes and Metabolism Program; Institut d'Investigació Biomèdica de Bellvitge (IDIBELL), Barcelona, Spain. [22]Centro de Investigación Biomédica en Red Fisiopatología de la Obesidad y la Nutrición (CIBEROBN), Instituto de Salud Carlos III, 28029 Madrid, Spain. [23]Department of Biochemistry and Physiology, School of Pharmacy and Food Sciences, Institut de Biomedicina de la Universitat de Barcelona (IBUB), Universitat de Barcelona, 08028 Barcelona,Spain. [24]Institució Catalana de Recerca i Estudis Avançats (ICREA), 08010 Barcelona, Spain. [25]Department of Basic Clinical Practice, Universitat de Barcelona, 08036 Barcelona, Spain.

*Correspondence: albagf@sund.ku.dk and pgarciaroves@ub.edu

‡ These authors contributed equally

Abstract

Metabolic plasticity is the ability of a biological system to adapt its metabolic phenotype to different environmental stressors. We used a whole-body and tissue-specific phenotypic, functional, metabolomic and transcriptomic approach to systematically assess metabolic plasticity in diet-induced obese mice after a combined nutritional and exercise intervention. Although most pathological features were successfully reverted, we observed a high degree of metabolic dysfunction irreversibility in visceral white adipose tissue, characterised by abnormal mitochondrial morphology and functionality. Despite two sequential therapeutic interventions and apparent global phenotypic recovery, obesity specifically triggered in visceral adipose a cascade of events progressing from mitochondrial metabolic and proteostatic defects to widespread cellular stress, which compromises its biosynthetic and recycling capacity. Our data indicate that obesity prompts a lasting metabolic fingerprint that leads to a progressive breakdown of metabolic plasticity in white adipose tissue, becoming a significant milestone in disease progression.

Keywords: Obesity, metabolic plasticity, visceral adipose tissue, mitochondrial dysfunction, exercise, caloric restriction, multi-organic approach, lifestyle intervention, aging-like phenotype, metabolic fingerprint.

Main text:

Introduction

Food availability, consumption surplus and sedentarism, predominant in most parts of the modern world, are the most significant environmental challenges that western societies are facing nowadays. According to the World Health Organization (WHO), in 2016, 650 million adults were suffering from obesity, with a growing incidence that had become a significant concern in healthcare (*1*). Moreover, obesity increases the risk for most common non-communicable diseases, including neurodegenerative and cardio-vascular diseases, cancer and type 2 diabetes (T2D). Tackling the biology underlying obesity-related TD2 is a challenge, as it is a multi-organic disease, from both pathological and etiological perspectives. Surgical, pharmacological and lifestyle-based interventions partially revert the obesity phenotype, although thwarted by their failure to sustain body weight loss and health benefits and frequent relapses (*2-4*). This failure to reverse obesity suggests that cellular and metabolic plasticity, interpreted as the ability of the cells to change and efficiently adapt their phenotypes to specific environmental cues, may be impaired. This phenomenon takes place in chronic conditions and diseases as well as in ageing, but whether obesity disrupts metabolic plasticity, notwithstanding therapeutic interventions, is still a conundrum.

In this context, the LiMa (Lifestyle Matters) project uses a comprehensive therapeutic approach focused on the systemic and tissue-specific impact of important environmental stressors (namely chronic overfeeding and physical inactivity). Our goal is to elucidate the reversibility and improvement of metabolic plasticity achieved by lifestyle interventions on the pathological changes in different organs caused by

obesity and insulin resistance. Here, we present an integrative multi-tiered approach to study the impact of lifestyle interventions on obesity, and reveal that obesity triggers a progressive breakdown of metabolic plasticity in white adipose tissue which is irreversible despite apparent phenotypic reversion.

Results

Combined nutritional and exercise intervention reverses HFD-induced phenotype

We investigated how reversible is diet-induced obesity through lifestyle intervention. Three experimental groups were defined: control group (Ctrl); HFD-induced obese and insulin-resistant group (HFD); and a third group (Int) which, included a nutritional and exercise intervention: specifically, a calorie restriction diet substitution (with poly- and mono-unsaturated rich oils and complex carbohydrates instead of saturated fats and simple sugars) combined with treadmill training, (*see methods section for detailed group description*). HFD group showed increased body weight (Figure 1A) by expanded fat volume (Figures 1B and 1C). Also, HFD mice showed increased triglyceride content in liver and soleus skeletal muscle (Figure 1D), along with disrupted metabolic flexibility (Figures 1E and 1F) and impaired glucose metabolism (Figures 1G-H) in comparison to the control group (Ctrl group). Glucose metabolism impairment was due to insulin resistance (Figure S1A) and pancreatic dysfunction evident by increased pancreas size, impaired glucose-stimulated insulin secretion,

131 both *in vivo* and *in vitro* (Figures 1H-L) and increased β cell mass (Figures 1K-L,
132 Figure S1B).

133 Combined nutritional and exercise intervention (Int group) reversed the observed
134 pathophysiology (Figures 1A-J) except for persistent hyperinsulinemia (both fasting
135 and after glucose stimulation) (Figure 1H), consistent with the maintained increase in
136 β cell mass after the intervention (Figures 1K-L, Figure S1B), even though *in vitro*
137 GSIS was fully recovered (Figure 1J). Altogether these results validated our diet-
138 induced obesity animal model and efficiency of the combined nutritional and exercise
139 intervention to revert obesity and partially the T2D phenotype.

140

141 **Tissue-specific pathological consequences of obesity and recovery after**
142 **combined nutritional and exercise intervention**

143 Next, we assessed the tissue-specific effect of the combined intervention on
144 metabolic plasticity. We used a three-tiered approach to elucidate the
145 pathophysiological impact of obesity-related insulin resistance in skeletal muscle,
146 liver, WAT, and hypothalamus. Specifically, this approach consisted of evaluating
147 mitochondrial respiration states (Mito); targeted expression profiles of genes related
148 to glucose and fatty acid metabolism, mitochondrial biogenesis, function, and stress
149 (Genes); and analysis of metabolites (Mets) (Figure 2A, Figures S2A-B and Suppl.
150 Table 1), investigating them in the tissues mentioned above and screening for the
151 presence or absence of reversibility.

152

153 Limited changes were observed in hypothalamus regardless of HFD-feeding or
154 intervention status. The intervention induced significant changes in glycolytic skeletal
155 muscle (tibialis anterior), consistent with the switch to an oxidative phenotype
156 promoted by the implementation of the exercise program. Mice on HFD-feeding
157 induced substantial metabolic changes (combined green and red bars) in oxidative
158 skeletal muscle (soleus). Of note, most of these metabolic changes were reverted
159 across the different tiers in muscle after the intervention (green bars). Liver and
160 epididymal WAT (eWAT) however, suffered profound metabolic changes upon HFD-
161 feeding (combined green and red bars) and even though the whole body improved
162 metabolic phenotype, these two tissues specifically exhibited sparse or non-reversion
163 (red bars) in all three phenotypical tiers (Figure 2A). To further assess the irreversible
164 loss of metabolic plasticity, we performed next-generation RNA sequencing (RNA-
165 seq) in liver and eWAT before and after the intervention. Differential expression
166 analysis revealed that, upon HFD-feeding, eWAT transcriptome was much more
167 perturbed than the liver transcriptome (7,451 vs 285 genes, respectively) (Figure 2B)
168 and that upon intervention, the eWAT transcriptome exhibited a lesser degree of
169 reversion (66% as compared to 94% in the liver) (Figures 2C and 2D).

170 Collectively, these results argued for a tissue-specific heterogeneous susceptibility to
171 obesity-induced defects in metabolic plasticity, and that eWAT specifically showed
172 the highest degree of irreversibility after a combined nutritional and exercise
173 intervention.

174

175

Incomplete remodeling of eWAT after the combined intervention

To further characterise the changes accounting for obesity-related metabolic irreversibility in eWAT, we studied the transcriptome. We identified downregulated (Figure 3A) and upregulated genes (Figure 3G) after HFD-feeding. Within the 3,869 downregulated genes, 1,036 recovered, 1,464 partially recovered, and 1,369 remained downregulated after the intervention (Figure 3A). Gene ontology enrichment analysis showed that non-reverted transcripts were related to biological processes such as biosynthesis, metabolism, and mitochondrial morphogenesis, organisation and transport (Figure 3B). In line with this, enrichment for cellular components identified genes involved in mitochondrial inner membrane (Figure S3A). Mitochondrial inner membrane is structured in *cristae*, whose density was significantly reduced after HFD-feeding and, unexpectedly, further decreased after the intervention (Figure 3C-D, Figure S3B). Decrease in cristae density was observed irrespective of maintenance of mitochondrial aspect ratio (Figure S3C). Additionally, processing of OPA1, a protein located in the inner mitochondrial membrane and master regulator of cristae architecture, revealed the same irreversible decrease after obesity and the intervention (Figure 3E). High-resolution respirometry studies in permeabilised eWAT confirmed the functional relevance of defects in cristae density revealing decreased respiratory capacity (Figure 3F).

From the 3,582 differentially upregulated genes after HFD-feeding (Figure 3G), 1,064 achieved a complete reversion, 1,389 were partially reverted and 1,129 transcripts did not change after the intervention. Gene ontology enrichment analysis of these non-reverted transcripts revealed biological processes associated with the immune

system and defense response (Figure 3H). To further validate these findings, we studied tissue immune infiltration in eWAT. The histological analysis revealed hypertrophied adipocytes surrounded by crown-like structures (composed by immune cells) in the HFD group (Figure 3J). Lastly, despite the improved systemic metabolic phenotype and the reduction of adipose tissue weight promoted by the intervention (Figure 3I), the histology of eWAT in these animals revealed a persistent alteration with the presence of dead adipocytes and massive immune cell infiltration (Figure 3J). These findings were corroborated by an increase in Caspase3- and Mac2-positive cells (Figure 4D, middle and lower panel, Figure S4C), markers of apoptosis and macrophages, respectively. Altogether, these results suggested an active eWAT remodeling after the intervention, potentially explaining the observed metabolic derangements.

Mitochondrial dysregulation persists in morphologically remodeled eWAT

The negative energy balance induced by exercise and nutritional intervention allowed for a global metabolic phenotypical recovery except for the increased pancreatic islets size (Figures 1K and 4A) and eWAT mitochondria dysfunction and immune cells infiltration (Figures 3 and 4A). After the partial achievements of sustained weight loss and improved physical fitness, we hypothesised that it would be necessary an extended milder intervention to recover the eWAT and pancreatic islets completely. Therefore, in a separate group of mice, we conducted an extra five weeks intervention following the same diet but undergoing pair-feeding and a less intense training program aiming at bodyweight maintenance (Figure 4A).

After this second phase of the intervention (Int2 group) (Figure S4A) the body weight was maintained, and glucose tolerance was comparable to the Int group (Figure S4B). Furthermore, the second intervention successfully decreased fasting insulin and glucose-stimulated insulin levels (Figure 4B) in line with reduced β cell mass (Figure 4C). The second intervention also improved eWAT atrophy and immune cell infiltration (Figure 4D, upper panel), along with a progressive reduction of Caspase3- and Mac2-positive cells (Figure 4D, middle and lower panel, and Figure S4C).

Adipose tissue expansion negatively influences tissue remodeling and functionality by limiting oxygen and nutrient supply to adipocytes. Oxygen limitation triggers an increase in succinate levels, which stabilises and activates HIF1-α, a master regulator of the cellular response to hypoxia and angiogenesis. Thus, we next examined whether the intervention had remodeled vascularisation parameters in eWAT. Unexpectedly, confocal microscopy studies revealed enhanced eWAT vascularisation after both interventions (Figures 4E and 4F). Also, analysis of critical mediators of angiogenesis in the Int2 group, revealed normalisation of *Hif1α* gene expression (Figure 4G), *Vegfα* and *Vegfr* gene expression (Figure S4D and S4E), and reduced levels of succinate (Figure 4H).

Additionally, we evaluated whether this eWAT morphological recovery after the second intervention was accompanied by reversion of gene expression patterns by RNA-seq. Specifically, out of the 1,129 transcripts upregulated after HFD and Int (Figure 3G), 82% had reverted to Ctrl values after Int2 (Figure 4I). Gene ontology analysis of these genes that recovered their expression revealed enrichment in biological processes linked to organelle and cytoskeleton organisation, immune

system, and inflammatory and defense response (Figure 4J and 4K). Besides that, from the 1,369 transcripts downregulated after HFD and Int (Figure 3A), 49% were recovered after Int2 while 51% still remained downregulated (Figure 4I). Gene ontology of the set of genes that were unable to restore their levels, showed, again, a significant enrichment in mitochondrial-related biological processes, such as electron transport chain, energy metabolism, biosynthesis, and mitochondrial organisation and transport (Figures 4O and 4P). Consistent with this result, mitochondrial respiratory capacity remained reduced after the second intervention (Figure 4Q). Altogether, these results demonstrate that metabolic and mitochondrial derangements in eWAT were resilient, and persisted even after resolution of morphological remodeling of the tissue, arguing for defects in mitochondria to be the main determinants of metabolic plasticity breakdown in eWAT.

Enduring mitochondrial derangements as a driver of WAT metabolic plasticity breakdown

Next, we speculated that additional transcriptional changes cascading downstream the HFD-induced phenotype during the interventions might help understand the observed metabolic scenario.

Three clusters were clearly defined amongst the genes irreversibly downregulated across the experimental groups: i) 893 genes irreversibly decreased with HFD-feeding (Figure 5A, Cluster A), ii) 601 genes irreversibly decreased from Int (Cluster B) and, iii) 678 genes with partially reduced expression in Int that became significantly

267 downregulated only after Int2 (Cluster C). Gene ontology revealed biological
268 processes and cellular components enriched in these three clusters (Figures 5B-C).
269 Genes irreversibly downregulated since the onset of diet-induced obesity and insulin
270 resistance (Cluster A) related to metabolic and biosynthetic processes at the
271 mitochondria and peroxisome level. Additionally, several other biological processes
272 enriched in Cluster A, such as lipid metabolism, adipocyte differentiation or apoptosis,
273 were further amplified in gene number size after the interventions (Clusters B and C,
274 inner circles). Genes downregulated after the first intervention (Cluster B) were also
275 related to additional processes such as RNA and glucose metabolism; protein folding
276 and transport to Golgi and mitochondria, as well as mitochondrial organisation. Of
277 significant relevance is the fact that previously downregulated genes were still
278 affected or further amplified even after the second intervention (Cluster C). Also,
279 genes from Cluster C showed new significant enrichments, such as in mitochondrial
280 organisation, proteasome complex and ribosomal biogenesis. Hence, these findings
281 indicate the irreversible course towards failure of transcriptional changes even after
282 reversal of the diet-induced obese and insulin resistant phenotype during the
283 sequential interventions. These changes lead to a progressive deterioration of eWAT
284 functionality and pointed to the mitochondria as the primary organelle affected,
285 triggering further transcriptional changes of genes involved in Golgi apparatus and
286 Endoplasmic Reticulum (Figure 5C).

287 In agreement with the alterations in the inner mitochondrial membrane,
288 cardiolipidomic analysis revealed that both HFD and Int2 group had decreased
289 monolysocardiolipin (MLCL) relative abundance, even when total cardiolipin (CL)

levels were already recovered (Figures 5D and 5E). Low MLCL levels likely indicate decreased cardiolipin remodeling rates as reported by CL deacylation-reacylation cycle genes being downregulated (i.e., *Pla2g6*, *Hsd17b10* and *Lpgat1*) or slightly increased (i.e., *Lclat1*) (Figures 5F-I). Also, a substantial reduction in mitochondrial DNA (mtDNA) copy number in eWAT (Figure 5M) supported previous findings and strengthened mitochondrial derangements as a critical component in WAT metabolic plasticity breakdown. Of note, other adipose depots such as subcutaneous WAT (scWAT, Figure 5J), liver (Figure 5K) and skeletal muscle gastrocnemius showed no changes in mtDNA (Figure 5L).

Finally, to identify the potential trigger of mtDNA reduction, we evaluated additional experimental groups in different dietary regimes aimed to overcome obesity. Intriguingly, all animals subjected to HFD-feeding also presented a decrease in mtDNA copy number regardless of the downstream intervention (namely intermittent fasting or switch to chow diet) (Figure 5M). On the contrary, such reduction was not observed in animals that were not previously obese but followed the same dietary regime (Figure 5M), suggesting that the stress induced by HFD could trigger a permanent damage. Collectively, our results reveal that phenotypically healthy mice after reversal of obesity show tissue-specific breakdown of metabolic plasticity, and highlight eWAT as the primary target. This breakdown is primarily characterised by a sequential and unresolved mitochondrial deterioration, further aggravating other cellular functions even after combined exercise and nutritional interventions.

Discussion

Obesity-related T2D is a chronic and degenerative disease that involves the interplay amongst and failure of several organs and tissues at both its onset and progression. This level of complexity requires a multidisciplinary and integrative experimental approach to capture interorgan communication and elucidate the vulnerability and resilience of organs leading to a global metabolic failure (*5, 6*). Thus, the current study uses a multidisciplinary and multi-organ approach to analyse an experimental combined intervention that proved to be successful in recovering nearly all phenotypical metabolic alterations in a diet-induced obese animal model. This animal model resembles the early stages of human obesity-related T2D pathology (*7, 8*). Moreover, this study provides valuable information in that it shows that lifestyle interventions are powerful treatments to overcome obesity and associated comorbidities. In addition, it allows for assessment of not only the phenotypic impact of HFD, but also how its metabolic fingerprint affects different tissues.

Our approach identifies the visceral WAT as the most affected tissue with metabolic derangements in obesity defined by its irreversible loss of functional plasticity despite apparently successful therapeutic interventions. An in-depth analysis of the global transcriptome in eWAT from obese mice reveals a generalised downregulation of metabolic processes mainly affecting mitochondria, and particularly its inner membrane and oxidative phosphorylation system (*9, 10*). The negative impact of chronic overfeeding in WAT mitochondria and how defective mitochondria performance influence WAT functionality has been extensively studied (*11-13*). The critical observation and novel finding here is that a combined nutritional and exercise

intervention, powerful to reverse obesity systemically and improve tissue-specifically into a healthy phenotype, leads to a long-lasting obesity-related mitochondrial deterioration in visceral WAT that becomes irreversible.

To elucidate whether this deterioration was due to an intrinsic mitochondrial defect or a consequence of a loss of tissue plasticity, we studied additional functional parameters. A considerable amount of evidence supports the requirement of an optimised degree of WAT expandability to preserve whole body homeostasis when faced with energy surplus challenges (*14*). Factors such as early angiogenesis and inflammation in response to mild tissue hypoxia are critical requirements for a healthy WAT expansion (*15, 16*). However, the chronicity of metabolic overload stress promoted by extended overfeeding periods can compromise tissue plasticity, creating a maladaptive response characterised by persistent oxidative damage, inadequate angiogenic response, severe hypoxia, adipocyte death, immune infiltration and fibrosis (*17*). Although these pathogenic events have been described, the mechanisms involved in the remodeling during the shrinkage promoted by weight loss remains controversial (*18-23*). On this respect, we observed evidence of hypoxia (namely accumulation of succinate levels and *Hif1-α* overexpression) in WAT of obese mice, without a parallel VEGF-mediated proper vascularisation, as well as marked dystrophy-like tissue architecture after weight loss. This suggests an evident defect in the remodeling mechanisms of adipose tissue. By implementing the second phase of intervention with maintenance of low body weight, all these parameters were normalised, thus indicating the completion of the remodeling process. Nonetheless, despite such improvements in tissue architecture and

vascularisation, mitochondrial defects were still present both at a transcriptional and functional level. Altogether, these results reinforce the novel finding of a permanent intrinsic mitochondrial damage in eWAT regardless of the tissue remodeling capacity (tissue plasticity).

The magnitude and specificity of the mtDNA reduction observed in eWAT amongst different experimental groups and tissues is a robust indicative sign of severe mitochondrial disturbances at the tissue specific-level and points at HFD-feeding as the driving force for such mitochondrial deterioration. Identification of the causative mechanisms leading to this irreversible structural, functional and transcriptional mitochondrial damage is challenging, due to the multifactorial components occurring under physiological conditions. Nonetheless, our findings reveal a series of events leading to mitochondrial damage and impaired tissue metabolic plasticity. It is well established that proper fine-tuning between mitochondrial biogenesis and recycling mediated by quality-control mechanisms is essential to ensure optimal functionality (*24*). However, critical perturbations in mitochondrial quality control could potentially cause cellular dysfunction involving protein import deficiencies and leading to cellular proteostatic defects and an ageing phenotype (*25*). In line with this, a recent paper by Yu *et al* demonstrated how, in the context of obesity, a disrupted protein import machinery in adipocytes is related to mitochondrial malfunction (*26*). Accordingly, the in-depth Gene Ontology analysis performed at different time-points shows that the downregulation of metabolic processes, initially confined to mitochondria, is spread to biological processes related to protein transport and folding, affecting other cellular compartments such as Golgi, Endoplasmic Reticulum

and the ubiquitin and proteasome system. Overall, these data are indicative of the spreading of original mitochondrial stress to other structures and processes, worsening global cellular stress and the ability to degrade and recycle damaged proteins or organelles. This finding is especially relevant in the context of a healthy phenotype at a systemic level after the intervention, in which HFD seems to trigger irreversible oxidative damage in eWAT that ultimately progresses and causes the breakdown of metabolic plasticity.

A reduced capacity to degrade or recycle cellular components could answer one of the most interesting questions arising from our results: why are such disrupted mitochondria still present in this tissue and not targeted for recycling through mitophagy processes? The observed defective cardiolipin remodeling adds insight in that direction. Indeed, cardiolipin remodeling plays a critical role in the link between oxidative stress (e.g. ROS) and mitochondrial dysfunction in different metabolic tissues (*27*). Under physiological conditions, this remodeling process links mitochondrial cardiolipin architecture to the phospholipid environment of the cell by a tissue-independent specificity mechanism that is not primarily controlled via gene expression (*28*). However, this holds as long as none of the essential components for cardiolipin remodeling becomes rate-limiting. In this respect, lysocardiolipin acyltransferase 1 (LCLAT1) has been suggested as a pivotal enzyme involved in the pathological remodeling of cardiolipin in various age-related pathological conditions including diet-induced obesity and T2D. Thus, LCLAT1 expression tendency to increase aggravates the vicious cycle among mitochondrial dysfunction, ROS damage, and defects in mitochondrial recycling capacity (*29-31*). Therefore, the

405 combination of different data sets not only evidences a deficiency in cristae formation
406 but also suggests a defective clearance of dysfunctional mitochondria as a plausible
407 explanation for this loss of metabolic plasticity.

408 In line with our findings, Hahn *et al* recently reported that, before any other tissue,
409 WAT of mice fed ad libitum exhibited significant age-related effects at a transcriptional
410 level (*32*). The study also identified a WAT-specific nutritional memory that impeded
411 its metabolic reprogramming when switched to calorie restriction. Although this study
412 was focused in late-life calorie restriction and longevity in mice, it revealed an ageing
413 phenomenon that shares similarities with the disease-oriented approach in our
414 research (namely diet-induced obesity). Altogether, we hypothesise that the stress
415 promoted by HFD might hasten adipocytes to enter in a premature ageing-like state
416 triggered by subsequent mitochondrial dysfunction, unsuccessful mitoprotein-
417 induced stress response and compromised cellular renewal capacity. Overall, all
418 these events agree with age-related processes reported in other chronic
419 degenerative diseases (*33, 34*).

420 To summarise, we demonstrate that nutritional and exercise interventions,
421 resembling a healthy lifestyle in humans, can revert a diet-induced obese and insulin
422 resistant phenotype in mice. However, the broad spectrum of data layers, studied
423 tissues and phenotypical characterisation performed in this study indicates a
424 hierarchy in the way organs are vulnerable and resilient. In this sense, it reveals a
425 metabolic plasticity breakdown in white adipose tissue. Thus, mitochondrial
426 deterioration in visceral WAT suggests an initial and critical point of no return in
427 metabolic disease progression, and therefore a relevant target for prevention and

428 early treatment. In the context of obesity, trigger of these processes could be
429 therefore avoided by implementing and advocating for early lifestyle interventions in
430 individuals at risk.

431

432 **Acknowledgements**

433 This work has been supported by Ministerio de Ciencia e Innovación (MICINN) Grant
434 BFU2011- 24679 (P.M.G.-R.); Instituto de Salud Carlos III (ISCIII) Grant PI15/00701
435 (P.M.G.-R.) cofinanced by the European Regional Development Fund ‘‘A way to
436 build Europe’’; Government of Catalonia Suport Grups de Recerca AGAUR 2017-
437 SGR-204 (to J.C.P. and P.M.G-R.), 2017-SGR-736 (to J.I.M.-S.) and 2017-SGR-896
438 (to A.A.-M., M.S.-P., and R.G.). M.M. was recipient of a MINECO grant RTI2018-
439 093864-B-I00. M.A.K. was funded by a Medical University of Innsbruck Start Grant.
440 M.C. was funded by the European Research Council (ERC) under the European
441 Union’s Horizon 2020 research and innovation programme (grant agreement
442 725004). L. H. was funded by MINECO grants SAF2013-45887-R, SAF2017-83813-
443 C3-1-R (granted to Dolors Serra (DS) and L.H.), co-funded by the European
444 Regional Development Fund, the Centro de Investigación Biomédica en Red de
445 Fisiopatología de la Obesidad y la Nutrición (CIBEROBN) (Grant CB06/03/0001 to
446 DS), the Government of Catalonia (2017SGR278 to DS), the Fundació La Marató
447 de TV3 (201627-30 to DS), the European Foundation for the Study of Diabetes
448 (EFSD)/Janssen-Rising Star and L’Oréal-UNESCO “For Women in Science”
449 research fellowships. P.M.G.-R. was a recipient of a Ramon y Cajal contract (RYC-
450 2009-05158) from MICINN. A.G-F. was a recipient of “Beca de Formació de

Personal Investigador de l'IDIBAPS" fellowship and she is currently supported by an unconditional donation from the Novo Nordisk Foundation (NNF) to NNF Center for Basic Metabolic Research (NNF18CC0034900). P.G-P. was a recipient of predoctoral fellowship from the Universitat de Barcelona (APIF-UB). E.S-R. was recipient of a predoctoral fellowship from Ministerio de Economia y Empresa (MINECO) grant BES-2013-062796. This work was partially developed at the Esther Koplowitz Centre (CEK, Barcelona, Spain).

Competing interests

The authors declare no competing interests.

Figure legends

Figure 1. HFD- and combined intervention-induced phenotype. A: Body weight for control (Ctrl, n=80), high fat diet-fed (HFD, n=70) and intervention (Int, n=46) groups. B: Quantification of fat volume by NMR imaging and 7Teslas scan representative images per phenotype (Ctrl n=4; HFD n=4; Int n=3). C: NMR representative images for each group for quantification in (B). D: Triglycerides (TG) levels in liver: Ctrl (n=8), HFD (n=7) and Int (n= 8); and soleus: Ctrl (n= 9), HFD (n= 8) and Int (n=8). E: Group-averaged respiratory exchange ratio (RER) deviation from the 24h median for each animal for Ctrl (n=11), HFD (n=10) and Int (n=6) for 48h in metabolic cages. F: Minimum and maximal values of deviation from median (RER variation, Figure E). G: Intraperitoneal glucose tolerance test (IGTT) for Ctrl (n=54),

HFD (n=48) and Int (n=12). H: Basal (t=0min) and 15min insulin levels during IGTT (Figure G) for Ctrl (n=15), HFD (n=19) and Int (n=13). I: Pancreas mean tissue weight for Ctrl (n=6), HFD (n=6) and Int (n=4). J: Glucose-stimulated (2.8 and 16.7mM) insulin secretion *in vitro* for pancreatic islets from animals in groups Ctrl (n=10), HFD (n=7) and Int (n=7). K: Immunohistochemistry representative images of pancreatic islets (nuclei-blue, insulin-red, glucagon-green) from animals in Ctrl, HFD and Int. L: Normalized pancreatic islet insulin area by pancreas section area for Ctrl (n=6), HFD (n=6) and Int (n=4). Ctrl: control; HFD: high fat diet-fed; Int: intervention. Data represented as mean ± SEM, ANOVA One-way and Post-hoc Tukey, *p<0.05, **p<0.01, ***p<0.001, and ****p<0.0001.

Figure 2. Tissue-specific effects of HFD-feeding and nutritional and exercise intervention. A: Schematic overview of the main processes taking place in tissues involved in obesity-related insulin resistance. Boxes highlight tissues analysed in this study (skeletal muscle, hypothalamus, liver and epididymal white adipose tissue, eWAT), where we represent the changes induced by HFD and Intervention on mitochondrial respiratory states (Mito), gene expression (Genes) and metabolites (Met). Each bar corresponds to the 100% of respiratory states/genes/metabolites analysed. Bands of different colors represent fractions of respiratory states/genes/metabolites showing different patterns of change: white – no changed; green – changed after HFD-feeding and reverted with intervention; red – changed after HFD-feeding and not reverted with intervention; grey – changed uniquely with intervention. B: Bar graph for RNA-seq in liver and eWAT. The black area represents

gene transcripts with changed expression after HFD-feeding. C-D: Percentage of gene transcripts reverted (green) or non-reverted (red) in liver (C) and eWAT (D) after the combined intervention.

Figure 3. Impairment of adipose tissue plasticity. A: Heatmap representing z-scores for RNA-seq cluster of transcripts downregulated after HFD-feeding (Ctrl n=8, HFD n=4, Int n=4). B: Gene ontology biological process (GOBP) enrichment analysis for the 1369 transcripts downregulated in HFD and Int. C: Electronic microscopy representative images of mitochondria cristae frequency, category 0, 1, 2 or 3 (see Methods section for category definition). D: Cristae density score according to categories detailed in C (Ctrl n=3, HFD n=4, Int n=4). E: Normalised protein expression of OPA1 (Ctrl n=7, HFD n=9, Int n=9). F: Mitochondrial respiratory states for eWAT homogenate (Ctrl n=13, HFD n=9, Int n=10). Substrates; P: pyruvate, M: malate, G: glutamate and S: succinate. Pathways; N: NADH electron transfer-pathway, S: Succinate dehydrogenase-linked pathway and NS: NS-linked pathways. Respiratory rates; L: Leak-state; P: Oxidative phosphorylation (OXHPOS)-state; E: Electron transfer (ETS)-state (*35*). G: Heatmap representing z-scores for RNA-seq cluster of transcripts upregulated after HFD-feeding (Ctrl n=8, HFD n=4, Int n=4). H: Gene ontology biological process (GOBP) enrichment analysis for the 1129 transcripts upregulated in HFD and Int. I: Epididymal WAT weight for control (Ctrl n=32, HFD n=32, Int n=26). J: Representative images for hematoxylin and eosin eWAT staining for each experimental group (Ctrl n=3, HFD n=4, Int n=4). Ctrl: control; HFD: high fat diet-fed; Int: intervention. Data represented

519 as mean ± SEM, ANOVA One-way and Post-hoc Tukey, *p<0.05, **p<0.01,
520 ***p<0.001, and ****p<0.0001.
521
522 **Figure 4. Mitochondrial deterioration in remodeled white adipose tissue**. A:
523 Scheme with the 4 experimental groups indicating the non-reverted parameters after
524 the first intervention (Int) and the rationale to then include a second intervention (Int2).
525 B: Basal (t=0min) and 15min insulin levels during IGTT (Ctrl n=28, HFD n=30, Int
526 n=14, Int2 n=10). C: Normalised pancreatic islet insulin area by total pancreas area
527 for Ctrl n=6, HFD n=6, Int n=4, Int2 n=4. D: Representative images for hematoxylin
528 and eosin eWAT, Caspase3- and Mac2-positive cells staining in eWAT for each
529 experimental group (Ctrl n=3-4, HFD n=4, Int n=3-4, Int2 n=4-5). E: Representative
530 of IB4-positive stained blood vessels in flat-mounted eWAT depots from each
531 experimental group. F: IB4-positive area quantification (Ctrl n=4, HFD n=3, Int n=4,
532 Int2 n=6). G: Normalized Hif1-α gene expression in eWAT (Ctrl n=8, HFD n=4, Int
533 n=4, Int2 n=4). H: Succinate metabolite levels in eWAT (Ctrl n=15, HFD n=13, Int
534 n=6, Int2 n=6). I: Heatmap representing z-scores for RNA-seq cluster of transcripts
535 upregulated after HFD-feeding and not recovered after Int (Ctrl n=8, HFD n=4, Int
536 n=4, Int2 n=4). J and K: Gene ontology biological processes (J) and cellular
537 components (K) enrichment of the genes clustered in 4I that revert after Int2. L: Z-
538 score for RNA-seq cluster of transcripts downregulated after HFD-feeding and not
539 recovered after Int (Ctrl n=8, HFD n=4, Int n=4, Int2 n=4). M and N: Gene ontology
540 biological processes (M) and cellular components (N) enrichment of the genes
541 clustered in 4L that revert after Int2. O and P: Gene ontology biological processes (O)

and cellular components (P) enrichment of the genes clustered in 4L that do not revert after Int2. Q: Mitochondrial respiratory states for eWAT homogenate (Ctrl n=13, HFD n=9, Int n=10, Int2 n=13). Substrates; P: pyruvate, M: malate, G: glutamate and S: succinate. Pathways; N: NADH electron transfer-pathway, S: Succinate dehydrogenase-linked pathway and NS: NS-linked pathways. Respiratory rates; L: Leak-state; P: Oxidative phosphorylation (OXHPOS)-state; E: Electron transfer (ETS)-state. Ctrl: control; HFD: high fat diet-fed; Int: intervention; Int2: second intervention. Data represented as mean ± SEM, ANOVA One-way and Post-hoc Tukey, *p<0.05, **p<0.01, ***p<0.001, and ****p<0.0001.

Figure 5. Metabolic plasticity breakdown in eWAT. A: Z-score for RNA-seq clusters of transcripts sequentially downregulated after HFD-feeding or the interventions, namely clusters A, B and C (Ctrl n=8, HFD n=4, Int n=4, Int2 n=4). B and C: Radar chart showing the gene ontology biological processes (B) and cellular components (C) enrichment after HFD-feeding (cluster A) or the interventions (clusters B and C). Pie proportion indicates gene size for each term or terms-groups indicated in the outside of the radar chart. Different colors represent different terms or terms-groups. D and E: Total cardiolipin (CL) abundance (D) and Monolysocardiolipin (MLCL) relative abundance (E) (Ctrl n=5, HFD n=10, Int2 n=8). F-I: Normalized gene expression of Pla2g6 (F), Lpgat1 (G), Lclat1 (H) and Hsd17b10 (I) in eWAT (Ctrl n=8, HFD n=4, Int n=4, Int2 n=4). J-M: Mitochondrial DNA (mtDNA) copy number in subcutaneous white adipose tissue (J), liver (K), skeletal muscle gastrocnemius (L) and epididymal WAT (M) (Ctrl n=6, HFD n=6, Int n=6, Int2 n=5,

565 Ctrl+IF n=8, HFD+Chow n=4, HFD+IF n=10, * indicate significant differences with Ctrl
566 group); *normalized by Ctrl mice* refers to eWAT Ctrl group (M). Ctrl: control; HFD:
567 high fat diet-fed; Int: intervention; Int2: second intervention; Ctrl+IF: control + dietary
568 intervention; HFD+Chow: high fat diet-fed + chow Ad libitum; HFD+IF: high fat diet-
569 fed + dietary intervention. Data represented as mean ± SEM, ANOVA One-way and
570 Post-hoc Tukey, *p<0.05, **p<0.01, ***p<0.001, and ****p<0.0001.

571

572 **Materials and Methods**

573 **Animals**

574 C57BL/6JOlaHSD male mice purchased from Envigo (Indiana, IN, USA) were kept
575 on a 12 h light/12 h dark cycle. Mice were assigned to two groups fed with different
576 diets for 16weeks: control group (*Ctrl*; fed with chow diet Teklad Global 14% Protein
577 Rodent Maintenance Diet by Envigo; final inclusion criteria: body weight (BW) < 33
578 g, fasting normoglycemia, fasting normal insulin, glucose tolerance and insulin
579 sensitivity); and a high-fat diet-fed group (*HFD*; D12451 by Research Diets, New
580 Brunswick, NJ, USA), final inclusion criteria: BW> 37 g, fasting hyperglycemia,
581 fasting hyperinsulinemia, glucose intolerance and insulin resistance). After 16 weeks
582 on HFD, a subgroup of *HFD* mice was assigned to the intervention group (*Int*, fed
583 with Preliminary Formula Rodent Diet with 45 kcal% Fat and Modification with
584 Flaxseed and Olive Oil by Research Diets, New Brunswick, NJ, USA); and a further
585 intervention was performed (*Int2*, fed with the same diet as the *Int* group), see
586 intervention details below. All animal procedures were approved by the local ethics

587 committee, Comitè Ètic d'Experimentació Animal at Universitat de Barcelona and
588 the Departament d'Agricultura, Ramaderia, Pesca, Alimentació i Medi Natural at the
589 Generalitat de Catalunya; complying with current Spanish and European legislation.

590

591 **Nutritional and exercise intervention**

592 Nutritional and exercise intervention (*Int* group) was initially for 5 weeks. The daily
593 energy intake was different during the first week compare to resting weeks, being
594 mice fed with 80% and then 100% in kcal of the daily energy intake determined for
595 a *Ctrl* animal, respectively. Intervention diet aimed at maintain energy content from
596 fat (45%) and included several nutritional modifications: replacement of sucrose by
597 corn starch and increase in mono- and polyunsaturated FA by changing oil origin
598 (flaxseed and olive oil were used instead of lard). Intervention diet was combined
599 with an exercise training program on a treadmill (Exer-6M Open Treadmill for Mice
600 and Rats with Shocker and Software 2-102 M/m Columbus Instruments; Columbus,
601 OH, USA). Acclimatisation was performed already during the first week of
602 intervention for 3 days prior 4 weeks of exercise training (5 days/week, 1 h/day). The
603 protocol was designed to increase gradually the speed until reaching a final
604 maximum speed of 20 m/min with a second level inclination (10º). In order to address
605 new experimental hypothesis, a second phase of intervention was implemented for
606 5 extra weeks (*Int2* group). Int2 maintained the diet (100% in kcal content of the daily
607 energy intake determined for a *Ctrl* animal) and the exercise program was adjusted
608 to an alternate-day workout, 1 hour/day with a fixed moderate speed (14-16 m/min)
609 and inclination (5%).

Body composition

Mice were scanned using Magnetic Resonance Imaging in a 7.0 Teslas BioSpec 70/30 horizontal (Bruker BioSpin, Ettlingen, Germany), equipped with an actively shielded gradient system (400 mT/m, 12 cm inner diameter). Animals were placed in a supine position in a Plexiglas holder with a nose cone for administering anesthetic (1.5% isoflurane in a mixture of 30% O_2 and 70% N_2O). Mice were scanned from below the head to the beginning of the tail, in 1.5 mm sections. A 3D reconstruction merging all the images was performed. Fat volume shown in white contrast was calculated merging the area values for each image. A Whole-body Composition Analyser (EchoMRI™, Houston, TX, USA) was used additionally.

Indirect calorimetry

TSE LabMaster (TSE Systems, Bad Homburg, Germany) was used as described previously (*36, 37*). Mice were acclimated for 24 h and then monitored for an additional 48h. Data was collected every 30 min for O_2 consumption and CO_2 production to determine energy expenditure with standard analysis software provided with the calorimeter system. Heat production was calculated by the abbreviated Weir equation ([3.94(VO_2) + 1.11(VCO_2)] 1.44) (*38*). Food and water intake, and locomotor activity were determined continuously for 48h. 30 min-RER values were averages for each animal in the same time point across 24 h. Median of these average for each animal was considered baseline, and the deviation to it was calculated, along with the maximal and minimum values.

633

634 **Glucose homeostasis *in vivo* functional assays**

635 Intraperitoneal Glucose Tolerance Test (IGTT) was performed after 16 h fasting (D-
636 Glucose at 2 g/kg of mouse BW). Blood glucose was measured before and 15, 30,
637 60 and 120 min after glucose administration. Insulin levels at time 0 and 15 were
638 measured by ELISA (90080 Crystal Chem Inc., Elk Grove Village, IL, USA)
639 according to manufacturer's instructions. Insulin Tolerance Test (ITT) was performed
640 after 4h fasting (insulin Humulin R 100 UI/mL Regular by Eli Lilly and Company
641 (Indiana, IN, USA), at 0.75 UI/kg of mouse BW). Blood glucose was measured using
642 a glucometer before and 15, 30, 60 and 120 min after insulin administration.

643

644 ***In vitro* glucose-stimulated insulin secretion (GSIS)**

645 Animals were anaesthetised and 2-3 mL of fresh collagenase XI solution was
646 injected in the clamped end of the bile duct inserted in the duodenum (Collagenase
647 from *Clostridium histolyticum*, Type XI, 2-5 FALGPA units/mg solid, >1200 CDU/mg
648 solid; C7657 Sigma, St. Louis, MI, USA) at 1000 U/mL in Hank's Balanced Salt
649 Solution (HBSS without MgCl2 and CaCl2; Gibco, Thermo Fisher Scientific,
650 Waltham, MA, USA). Pancreas tissue was then collected and incubated at 38ºC for
651 14 min before manual agitation, and after two washes with ice-cold HBSS containing
652 CaCl2 (HBSS, Sigma, St. Louis, MI, USA), the pellet was resuspended in 7 mL and
653 filtered (Cell Strainer 70 um Nylon; BD Falcon, Bedford, MA, USA). The islets in the
654 filter were washed twice with HBSS and plated in a RPMI solution by inverting the

filter (RPMI, Gibco, Thermo Fisher Scientific, Waltham, MA, USA, supplemented with 2 mM L-glutamine, 1000 units/mL of both penicillin and streptomycin, Thermo Fisher Scientific, Waltham, MA, USA, and 10% FBS, Biosera, Manila, Philiphines). About 70 islets per animal were handpicked for each animal and cultured overnight in RPMI media, and then splitted in tubes of 15. To measure *insulin secretion*, islets were pre-incubated in agitation for 30 min in freshly prepared KRBH secretion solution ($NaCl_2$ 140 mM, KCl 4.5 mM, $MgCl_2 \cdot 6H_2O$ 1mM, HEPES 20 mM, $CaCl_2$ 2.5 mM, 0.1%BSA, with 2.8 mM glucose) and then incubated in KRBH solution with 2.8 mM or 16.7 mM glucose for 1h. Supernatants were collected and for *insulin content*, remaining islets were lysed in glacial acetic (5.75% (v/v) in 0.1%BSA) following an overnight freezing cycle at -80ºC, warm them at 95ºC for 10 min, then centrifuging them at 4ºC and collecting the supernatant. Insulin levels were measured in supernatants from both *insulin secretion* and *insulin content* assays, by ELISA (Crystal Chem Inc., Elk Grove Village, IL, USA) according to manufacturer's instructions. Insulin secretion was normalised by insulin content.

Analytical measurements

For triglyceride measurements, lipids were extracted from tissue homogenates (100 mg of tissue in SDS 0.1%) using chloroform:methanol (2:1) to extract the organic phase pellet and resuspend it in ethanol. Triglyceride Reagent, Free Glycerol Reagent and Glycerol Standard Solution (T2449, F6428, G7793 Sigma, St. Louis, MI, USA) were used according to a modified protocol from the one provided by manufacturers in liver and skeletal muscle. Briefly, Free Glycerol Reagent was

678 added to samples and standards in a 96-well microplate (NUNC, Denmark)
679 incubated at 37ºC for 5 min. Absorbance at 540 nm was read before and after the
680 addition of Triglyceride Reagent (Synergy HT Multi-Mode Microplate Reader,
681 BioTek, Winooski, VT, USA).

682

683 **Pancreas morphometry studies**

684 Collected pancreas tissue was fixed overnight in formalin at 4ºC, dehydrated and
685 embedded in parafin blocks (Embedding Center, Leica, Buffalo Grove, IL, USA), cut
686 in 4 μm sections separated by 150 μm (Rotary Microtome, Leica, Buffalo Grove, IL,
687 USA) and placed in Poly-L-Lysine treated microscope slides. Paraffin was removed,
688 and the tissue was permeabilised in PBS1X+1%Triton, blocked with 3% BSA in
689 PBS1 and incubated overnight at 4ºC with primary polyclonal antibodies for glucagon
690 and insulin (Dako, Agilent, Santa Clara, CA, USA) (Table S8). Secondary antibodies
691 were conjugated with Alexa Fluor®488 and Alexa Fluor®555 (Life Technologies,
692 Carlsbad, CA, USA) (Table S8) and Hoechst was used for nuclei staining. An
693 inverted-fluorescence microscope with camera (Leica, Buffalo Grove, IL, USA) and
694 ImageJ were used to obtain and to measure the number and area of positive cells,
695 respectively. The pancreas section was stained with tolonium chloride to measure
696 the area and normalise the values.

697

698

699

Gene expression

50-100 mg of tissue were homogenised in 1 mL TRI Reagent (93289 Sigma, St. Louis, MI, USA) using magnetic beads (0.5 mm diameter ZrO_2 for BulletBlender, NextAdvance, Troy, NY, USA) in a BulletBlender following manufacturer instructions for each tissue. For adipose tissue samples, a centrifugation was performed at this point to discard the surface layer. Supernatants were collected for RNA extraction according to manufacturer's instructions. cDNA was obtained using the High Capacity cDNA Reverse Transcription Kit (4368814 Applied Biosystems, Thermo Fisher Scientic, Waltham, MA, USA). cDNA dilution for each tissue was optimised. RT-PCR assays were performed in 384-well plates (Attendbio, Cerdanyola del Valles, Spain) using the 7900HT RT-PCR system (Thermo Fisher Scientific, Waltham, MA, USA) and the commercial reagents *Premix Ex Taq*™ (BN2001 TaKaRa Bio Inc., Kusatsu, Japan) according to recommended conditions. All Taqman® probes were obtained from Applied Biosystems (Table S8). A standard curve of pooled samples was used for quantification.

Protein content

Tissues were homogenised with magnetic beads as described above and lysed using 300 uL of lysis buffer (Na_2HPO_4 10 mM, NaF 10 mM, Tris pH 7.5-8 50 mM, EDTA 5 mM, NaCl 150 mM and Triton X-100 150 mM) with the addition of a protease inhibitors cocktail (Roche), and mechanically disrupted through freeze-thaw cycles. Supernatants were collected for protein quantification and diluted at a given

722 concentration in lysis buffer and Laemmli sample buffer 4X. Criterion XT Bis-Tris Gel
723 (BioRad, Hercules, CA, USA) were used for electrophoresis. Transfer of the proteins
724 to the PVDF membranes was performed using the Trans-Blot Turbo™ Transfer
725 System (BioRad, Hercules, CA, USA). Membrane was blocked for 1h at RT (5% milk
726 in TBS-T) and incubated overnight at 4ºC with primary antibodies (Table S8).
727 Secondary antibodies were incubated for 1h at RT. Pierce™ ECL Western Blotting
728 Substrate (Thermo Fisher Scientific, Waltham, MA, USA) was used in an
729 ImageQuant LAS 4000 (GE Healthcare, Chicago, IL, USA) for imaging of blots by
730 chemiluminescence. ImageQuant TL Software (GE Healthcare, IL, USA) was used
731 for the blot quantification.

732

733 **High-resolution respirometry**

734 Mitochondrial respiration was assessed by high-resolution respirometry (HRR) in
735 glycolytic and oxidative skeletal muscles, hypothalamus, liver and white adipose
736 tissue. For sample preparation, each tissue was homogenised and permeabilised in
737 fresh conditions as described in (*39*). Experiments were performed in Oxygraph-2k
738 system (Oroboros Instruments, Innsbruck, Austria) according to an established
739 substrate-uncoupler-inhibitor titration (SUIT) HRR protocol
740 (https://www.mitofit.org/index.php/SUIT-008), where the nomenclature used is
741 defined (see further details in (*35*)). Briefly, LEAK respiration was measured in the
742 presence of the NADH (N)-linked substrates Pyruvate (5mM) and Malate (2mM).
743 Oxidative phosphorylation capacity was then determined by the addition of ADP

744 (5mM) at saturated concentrations, and cytochrome C (10μM) was added to assess
745 the integrity of the mitochondrial outer membrane before the addition of Glutamate
746 (10mM). Then, Succinate (10mM) was added to stimulate the succinate (S)-linked
747 pathway, allowing the convergent electron flow through both pathways
748 simultaneously. Subsequent titration of the uncoupler carbonyl cyanide p-trifluoro-
749 methoxyphenyl hydrazine (FCCP, 0.5μM) was then performed to assess maximal
750 non-coupled Electron Transfer (ET)-respiratory capacity mediated by NS-linked
751 pathways. ET-respiratory capacity mediated uniquely by S-pathway was also
752 evaluated inhibiting complex I by the addition of Rotenone (0.5μM). Finally, residual
753 oxygen consumption (ROX) was determined by the inhibition of complex III adding
754 Antimycin A (2,5μM) and this value was subtracted from O2 flux as a baseline for all
755 respiratory states. The O2k-Software DatLab 7.4 was used for real-time data
756 acquisition and analysis. Oxygen flux values were expressed relative to tissue wet
757 weight per second (JO2, pmol mg-1 s-1).

758

759 **Adipose tissue histology**

760 Histological examination was done using 4 μm thick sections from formalin-fixed
761 paraffin-embedded tissue samples, which were stained with hematoxylin and eosin
762 (H&E) at the Pathology Department of the Hospital Clinic of Barcelona. Two-four μm
763 thickness sections from paraffin embedded samples were used for
764 immunohistochemistry at the Tumour Bank of the HCB-IDIBAPS Biobank (IDIBAPS,
765 Barcelona) using the Leica Microsystems' Bond-max™ automated immunostainer

766 together with the Bond Polymer Refine Detection System (Leica Microsystems,
767 Spain). Briefly, tissue sections were deparaffinised, and pretreated for antigen
768 retrieval with citrate buffer, pH 6.0 20 minutes for Caspase 3 and Mac2. For
769 macrophage immunostaining: primary monoclonal rat anti-murine antibody to Mac2
770 (Cedarlane Labs, Burlington, Ontario, Canada) (Table S8) was used at 1:40,000 for
771 one hour, combined with a secondary rabbit anti-rat Ig at 1:3,000. For apoptosis:
772 monoclonal rabbit anti-murine Caspase3 antibody (Cell Signaling Technology,
773 Danvers, MA, USA) (Table S8) was used at 1:500 for one hour. Finally, samples
774 were developed with diaminobenzidine and counterstained with hematoxylin.
775
776 **Mitochondria electron microscopy**
777 Anesthetized animals were perfused transaortically with 50 mL heparinized saline
778 (10mg/L heparin in saline (0.9% NaCl)) followed by 100 mL of fixative solution
779 (glutaraldehyde 2.5% + paraformaldehyde 2% in phosphate buffer 0.1 M pH=7.4).
780 Once perfused, a small piece of adipose tissue was collected and placed on vials
781 with fixative solution for 24 h. Samples were rinsed four times with phosphate buffer,
782 postfixed with 1% osmium tetroxide (EMS, Hatfield, PA, USA) for 2 h and rinsed with
783 milliQ water. Samples were then dehydrated in an acetone series (50%, 70%, 90%,
784 96% and 100%, for 10 min each), and infiltrated and embedded in Epon resin (EMS,
785 Hatfield, PA, USA). Ultrathin sections of 60nm in thickness were obtained using a
786 UC6 ultramicrotome (Leica, Buffalo Grove, IL, USA) and were stained with 2% uranyl
787 acetate and lead citrate. Sections were observed in a Jeol 1010 (Gatan, Abitasu
788 Yaesu, Japan) equipped with a tungsten cathode and Images were acquired at 80
789 kv with a CCD Megaview 1kx1k. Mitochondrial cristae density was evaluated

790 distributing mitochondria in 4 categories: 0-not visible cristae; 1-very few cristae; 2-
791 half of the mitochondria shows cristae, 3-equaly distributed cristae.
792

793 **Whole mount adipose tissue immunostaining and vessel area quantification**

794 Approximately 3 mm^3 cubes of adipose tissue were cut from each sample and
795 permeabilised for 1h with phosphate buffer saline (PBS) and 1% Triton-x 100.
796 Afterwards, tissues were blocked with blocking buffer (PBS + 0,3% Triton-x 100 +
797 5% goat serum) for 2 h at room temperature. Primary antibody (Isolectin GS-B4 568,
798 Invitrogen, Thermo Fisher Scientic, Waltham, MA, USA) (Table S8) diluted (1:2000)
799 in blocking buffer was incubated overnight at room temperature, with over day
800 washings with PBS + 0,3% Triton-x 100. Afterwards, samples were clarified using
801 90% glycerol at 4°C overnight. Samples were stored in ProLong™ Gold Antifade
802 Reagent (P36930 Invitrogen, Thermo Fisher Scientic, Waltham, MA, USA) with
803 DAPI. Images were taken with a Leica SP5 confocal microscope using 20X and 40X
804 objectives (Leica, Buffalo Grove, IL, USA). All images are maximal z-stack
805 projections. Images were processed using Volocity, Fiji and Adobe Photoshop CS5.
806 Vessel density was quantified by measuring isolectin-B4 positive area, within a fixed
807 square template, using the ImageJ software.
808

809 **Phospholipid extraction**

810 White adipose tissue (WAT) was homogenised in PBS of which 5% was removed to
811 determine protein content via Bradford assay. Next, lipids were extracted twice from

812 homogenate with 2:1 chloroform:methanol (Folch method) containing 0.5 µM
813 $CL(14:0)_4$ as internal standard and dried under N_2 flow. Due to the high content of
814 neutral lipids in WAT, phospholipids were separated by solid-phase extraction using
815 Sep-Pak C18-columns (Waters Associates, Milford, MA, USA). Briefly, the lipid
816 extract was re-suspended in 1 mL chloroform, applied on the column and washed
817 thrice with 1 mL chloroform to elute neutral lipids. Phospholipids were eluted by
818 quadruple addition of 2:1 chloroform:methanol and quadruple addition of methanol,
819 collected and dried under N_2 flow.

820

821 **LC-MS/MS analysis of CL MLCL**

822 CL analysis was performed as described in (*40*). Phospholipid extracts were
823 dissolved in HPLC starting condition and subjected to HPLC-MS/MS analysis.
824 Separation was achieved by reversed-phase HPLC with an Agilent Poroshell 120
825 EC-C8 2.7 µm 2.1x100mm column (Agilent Technologies, Santa Clara, CA, USA)
826 on a Dionex Ultimate 3000 HPLC (Thermo Fisher Scientific, Waltham, MA, USA,
827 50°C column oven, 0.4 mL/min flow) with running solvent A (60/40 Acetonitrile/H_2O,
828 10 mM ammonium formate, 0.2% formic acid) and running solvent B (90/10
829 Isopropanol/Acetonitrile, 10 mM ammonium formate, 0.2% formic acid). Analytes
830 were measured using a LTQ Velos MS (Thermo Fisher Scientific, Waltham, MA,
831 USA) operated in negative ESI mode (3.8kV, 275°C capillary temperature, 460-1650
832 m/z) and data-dependent MS2 acquisition. Thermo raw data was converted to open-
833 source MZML format and Peaks were integrated in MZmine2 (*41*). Identification was
834 based on a combination of accurate mass, (relative) retention times, and

835 fragmentation spectra, compared to a library of standards. Data was corrected for
836 internal standard, normalised on protein content, quantified using an external dilution
837 series ($CL(14:0)_4$, $CL(18:1)_4$) and further analysed by an in-house pipeline in R.
838 Significance was calculated using a one-way ANOVA with post hoc Tukey
839 correction.

840

841 **Quantification of mtDNA copy number**

842 Mitochondrial DNA (mtDNA) content was determined by qPCR of total DNA
843 extracted. NucleoSpin Tissue DNA purification kit (Macherey-Nagel, Dueren,
844 Germany) was used to extract total DNA from adipose tissue according to
845 manufacturer's protocol, and NanoDrop 1000 Spectrophotometer (Thermo Fisher
846 Scientific, Waltham, MA, USA) to quantify DNA concentration. GoTaq® qPCR
847 MasterMix (Promega, Madison, WI, USA) and 3ng of DNA sample were combined
848 to amplify both mtDNA and nuclear DNA by 7900HT RT-PCR system (Thermo
849 Fisher Scientific, Waltham, MA, USA) using the following primers; cytochrome C
850 subunit 2 (*mt-Co2* Fw: CTACAAGACGCCACAT – *mt-Co2* Rv:
851 GAGAGGGGAGAGCAAT), 12S rRNA (*Mt-Rnr1*Fw:
852 CTTCAGCAAACCCTAAAAAGG – *Mt-Rnr1*Rv: GCGTACTTCATTGCTCAATTC)
853 and succinate dehydrogenase subunit A (*Sdha* Fw: TACTACAGCCCCAAGTCT -
854 *Sdha* Rv: TGGACCCATCTTCTATGC). mtDNA content is referred to nuclear DNA
855 (nDNA) as the copy number ratio of mtDNA to nDNA.

856

857

858 **Metabolomics sample preparation**

859 Pulverised liver tissue (50-100 mg) was mixed with ice-cold acetonitrile:water (1:1)
860 and ultrasonicated, and the combined supernatant aqueous phases of 3 repetitions
861 were frozen and lyophilised. The resultant pellet was dried and extracted with
862 chloroform:methanol (2:1) by ultrasonication. The supernatant organic phase was
863 collected and dried under N_2 stream. Pulverised white adipose (30-70 mg),
864 gastrocnemius (20-40 mg) and hypothalamus (10-25 mg) tissue was mixed with
865 methanol and ultrasonicated before chloroform was added in two steps to final 1:1.
866 Water was added 1:2:2 (water:methanol:chloroform) and the aqueous upper phase
867 containing water and methanol and the organic lower phase were collected
868 separately. An aqueous extract was dissolved in D2O (containing 0.67 mM
869 trisilylpropionic, TSP) and the organic extract was reconstituted in $CDCl_3/CD_3OD$
870 (2:1) solution (containing 1.18 mM tetramethylsilane, TMS). The supernatant of both
871 phases was transferred into 5mm NMR tubes.

872

873 **Nuclear Magnetic Ressonance (NMR) metabolomics analysis**

874 ^{1}H-NMR spectra were recorded at 310K on a Bruker Avance III 600 spectrometer
875 (Bruker, Billerica, USA) operating at a proton frequency of 600.20MHz using a 5mm
876 CPTCI triple resonance (^{1}H, ^{13}C, ^{31}P). One-dimensional ^{1}H pulse experiments of
877 aqueous samples were performed. In order to suppress the residual water peak the
878 experiments were recorded using the *NOESY-presat* sequence, with the mixing time
879 set at 100ms. A 75Hz-power irradiation was applied during recycling delay and

mixing time to presaturate the solvent. A total of 256 transients were collected into 64 k data points for each ^{1}H spectrum, being the spectral width set as 12 kHz (20 ppm). The exponential line broadening applied before Fourier transformation was of 0.3Hz. In order to remove the residual water moisture of deuterated methanol, lipidic samples were measured using a simple presaturation sequence. Thus, a 50Hz-power irradiation was used during recycling delay and mixing time to presaturate the solvent. Again, 256 transients were collected into 64 k data points for each ^{1}H spectrum, being the spectral width set as 12kHz (20 ppm). The exponential line broadening applied before Fourier transformation was also here of 0.3Hz. Of note, the frequency domain spectra were manually phased and baseline-corrected using TopSpin software (version 2.1, Bruker, Billerica, USA).

NMR data analysis

All the acquired ^{1}H NMR spectra were phased, baseline-corrected, and referenced to the chemical shift of TSP or TMS signal at 0 ppm. For metabolic identification, references of pure compounds from the metabolic profiling AMIX spectra database (Bruker, Billerica, USA), human metabolome database (HMDB), and Chenomx databases were used (Chenomx Inc. Edmonton, Canada) . After baseline correction, specific ^{1}H NMR regions identified in the spectra were integrated for each extraction method entering the study using the AMIX 3.8 software package. Then, each integration region was normalised using the tissue weight used from each sample.

Data (pre-) processing, data analysis, and statistical calculations were performed in RStudio (R version 3.0.2).

RNA-Seq data processing and differential expression analysis

RNA samples from 20 WAT samples (Ctrl n=8, HFD n=4, Int n=4 and Int2 n=4) as well as 12 liver tissue samples (Ctrl n=4, HFD n=4 and Int n=4) were sequenced by standard Illumina protocol to create raw sequence files (.fastq files), which underwent quality control analysis using FastQC (http://www.bioinformatics.babraham.ac.uk/projects/fastqc/). We aligned the quality checked reads to the Mouse Genome, version July 2007 (NCBI37/mm9) using TopHat version 2.1.1 allowing for unique alignments to the genome and up to two mismatches. The resulting alignments were summarised by Ensembl gene identifiers to evaluate number of uniquely aligned reads per transcript and per sample (raw read counts).

RNA-seq data were analysed using the limma package version 1.8.2 available through the Bioconductor open source. The raw read counts were used as input to form a DGEList object combining the counts and associated annotation. Scale normalisation was applied and the calculation of normalised signal was performed by voom function of the limma package (*42*) available through the Bioconductor open source software. This differential expression analysis was performed pair-wise between different experimental conditions, but per each tissue type separately (FDR<0.05). First, we identified genes either up- or downregulated in HFD conditions

as compared to controls. Then, we explored the expression modulation of these two sets of genes after first intervention (Int). We could determine three distinct patterns: 1) genes fully recovered (with differential expression between HFD and Int but no significant difference in expression between controls and Int); 2) genes partially recovered (not reaching the same expression level as in control conditions but showing the recovering tendency between HFD and Int); 3) genes not recovered (that continue to be differentially expressed between Int and controls, with no significant difference in expression between HFD and Int). In the case of WAT, for the third, not recovered category, we performed similar expression patterns analysis using the data of second intervention (Int2), defining the genes that recovered or not after this additional experimental step.

Gene Ontology analysis

For different gene sets, GO enrichments were performed using the GOstats R package (*43*), separately for biological processes and cell compartments related GO terms. Significant GO terms ($p<0.0001$) were further summarised together by ReVigo software (*44*) in order to represent them as semantic-similarity scatter plot of the most significant GO terms, with a modification of the script to represent the GO enrichment values as dot size. To represent the cascade of GO terms affected in different steps of the experiment (HFD, Int and Int2, Figure5), we combined a biological and semantic approach, merging those GO terms that contained the same genes and that were related to the same biological process or cell compartment. In this analysis, general, ancestor GO terms (the highest level in GO terms tree;

typically containing over 500 genes) as well as very specific GO terms (typically containing less than 5 genes) were excluded, in order to obtain a clearer view of the GO terms dynamics throughout three different experimental conditions.

Database and pattern data analysis

Gene expression (transcriptomics), metabolites content (metabolomics) and mitochondrial respiration states (high-resolution respirometry) patterns were analysed and are presented in Figure 2. A Content Management System (CMS) dynamic database with a front-end user interface or a content management application (CMA) (idibaps.seeslab.net) was created along with a Content Delivery Application (CDA) that compiles all the information and updates the website. An entry for each mouse was generated including both *phenotypical information* (e.g., animal identification, group (Ctrl, HFD or Int), body weight, glucose levels (IGTT, ITT), etc) and *specific-tissue data* (e.g., mitochondrial respiratory values, gene expression data, protein content data, targeted metabolomics data, etc). Python scripts allowed correlation and comparison analysis of all the attributes entered in the database, which were structured in a pandas. DataFrame (http://pandas.pydata.org/) generated from the database. NumPy and SciPy were used for working with multi-dimensional arrays and matrices as well as for calculating high-level mathematical functions. Matplotlib was used for graphical representations (i.e., stacked bar plot). Pattern data analysis: to visually show the proportion of parameters that were reversed after the intervention we defined a 3-point vector for each parameter (e.g., gene expression, metabolite, mitochondrial respiration state)

969 in which the 3 points correlated to the mean of this given parameter for 1) Ctrl group
970 2) HFD-fed group and 3) Int group (i.e., *parameter=[Ctrl mean, HFD mean, Int*
971 *mean]*). Mann-Whitney comparisons were used to compare the groups. Once the
972 significant differences were calculated, different patterns were defined: green for a
973 reversion pattern after the intervention; red for no reversion in the intervention group,
974 so the mean value in the HFD group, which is significantly different from the Ctrl
975 group, is not different in comparison to the Int group; and grey for a difference in the
976 Int group in comparison to the other two groups, between the ones there is no
977 difference. Once these patterns were defined for gene expression, metabolites and
978 mitochondrial respiration states in skeletal muscle (gastrocnemius, soleus and
979 tibialis anterior), hypothalamus, liver and epididymal adipose tissue, stacked bar
980 plots were used to visualise the relative percentage of all the
981 genes/metabolites/respiratory states falling in the different patterns.

982

983 **Statistical analysis**

984 Results are expressed as Mean±SEM. The statistical significance among the three
985 experimental groups was assessed using one-way ANOVA, and differences
986 between means were subsequently tested by Tukey post-hoc test. Data curation
987 involved the removal of values that were ±2 standard deviation (SD) in punctual
988 situations. A p-value <0.05 was considered significant in all cases, meaning a
989 confidence interval of 95% and setting significance level at $\alpha=0.05$. Tendencies with
990 p-value between 0.05 and 0.07 are also indicated. All statistical analyses were
991 performed using GraphPad 6 (GraphPad Software, Inc. La Jolla, CA, USA).

Lead Contact

Further information and requests for resources should be directed to and will be fulfilled by the Lead Contact, Pablo M. Garcia-Roves (pgarciaroves@ub.edu).

References

1. WHO, https://www.who.int/en/news-room/fact-sheets/detail/obesity-and-overweight.
2. M. Bluher, Obesity: global epidemiology and pathogenesis. *Nat Rev Endocrinol* **15**, 288-298 (2019).
3. M. A. van Baak, E. C. M. Mariman, Mechanisms of weight regain after weight loss - the role of adipose tissue. *Nat Rev Endocrinol* **15**, 274-287 (2019).
4. S. B. Heymsfield, T. A. Wadden, Mechanisms, Pathophysiology, and Management of Obesity. *N Engl J Med* **376**, 1492 (2017).
5. F. Bäckhed *et al.*, The next decade of metabolism. *Nature Metabolism* **1**, 2-4 (2019).
6. DIAMAP, https://www.diamap.eu/roadmap/domain/detail/3.
7. V. A. Fonseca, Defining and characterizing the progression of type 2 diabetes. *Diabetes Care* **32 Suppl 2**, S151-156 (2009).
8. J. E. Galgani, C. Moro, E. Ravussin, Metabolic flexibility and insulin resistance. *Am J Physiol Endocrinol Metab* **295**, E1009-1017 (2008).
9. L. Wilson-Fritch *et al.*, Mitochondrial remodeling in adipose tissue associated with obesity and treatment with rosiglitazone. *J Clin Invest* **114**, 1281-1289 (2004).
10. J. X. Rong *et al.*, Adipose mitochondrial biogenesis is suppressed in db/db and high-fat diet-fed mice and improved by rosiglitazone. *Diabetes* **56**, 1751-1760 (2007).
11. A. De Pauw, S. Tejerina, M. Raes, J. Keijer, T. Arnould, Mitochondrial (dys)function in adipocyte (de)differentiation and systemic metabolic alterations. *Am J Pathol* **175**, 927-939 (2009).
12. S. Boudina, T. E. Graham, Mitochondrial function/dysfunction in white adipose tissue. *Exp Physiol* **99**, 1168-1178 (2014).
13. J. H. Lee *et al.*, The Role of Adipose Tissue Mitochondria: Regulation of Mitochondrial Function for the Treatment of Metabolic Diseases. *Int J Mol Sci* **20**, (2019).
14. S. Carobbio, V. Pellegrinelli, A. Vidal-Puig, Adipose Tissue Function and Expandability as Determinants of Lipotoxicity and the Metabolic Syndrome. *Adv Exp Med Biol* **960**, 161-196 (2017).
15. K. Sun *et al.*, Dichotomous effects of VEGF-A on adipose tissue dysfunction. *Proc Natl Acad Sci U S A* **109**, 5874-5879 (2012).
16. I. Wernstedt Asterholm *et al.*, Adipocyte inflammation is essential for healthy adipose tissue expansion and remodeling. *Cell Metab* **20**, 103-118 (2014).
17. C. Crewe, Y. A. An, P. E. Scherer, The ominous triad of adipose tissue dysfunction: inflammation, fibrosis, and impaired angiogenesis. *J Clin Invest* **127**, 74-82 (2017).
18. F. P. Hoevenaars *et al.*, Adipose tissue metabolism and inflammation are differently affected by weight loss in obese mice due to either a high-fat diet restriction or change to a low-fat diet. *Genes Nutr* **9**, 391 (2014).
19. D. Y. Jung *et al.*, Short-term weight loss attenuates local tissue inflammation and improves insulin sensitivity without affecting adipose inflammation in obese mice. *Am J Physiol Endocrinol Metab* **304**, E964-976 (2013).
20. A. Kosteli *et al.*, Weight loss and lipolysis promote a dynamic immune response in murine adipose tissue. *J Clin Invest* **120**, 3466-3479 (2010).
21. B. Liu *et al.*, Intermittent Fasting Improves Glucose Tolerance and Promotes Adipose Tissue Remodeling in Male Mice Fed a High-Fat Diet. *Endocrinology* **160**, 169-180 (2019).
22. J. Schmitz *et al.*, Obesogenic memory can confer long-term increases in adipose tissue but not liver inflammation and insulin resistance after weight loss. *Mol Metab* **5**, 328-339 (2016).

23. B. F. Zamarron *et al.*, Macrophage Proliferation Sustains Adipose Tissue Inflammation in Formerly Obese Mice. *Diabetes* **66**, 392-406 (2017).
24. S. Michel *et al.*, Crosstalk between mitochondrial (dys)function and mitochondrial abundance. *J Cell Physiol* **227**, 2297-2310 (2012).
25. F. Boos, J. Labbadia, J. M. Herrmann, How the Mitoprotein-Induced Stress Response Safeguards the Cytosol: A Unified View. *Trends Cell Biol* **30**, 241-254 (2020).
26. Y. A. An *et al.*, Dysregulation of Amyloid Precursor Protein Impairs Adipose Tissue Mitochondrial Function and Promotes Obesity. *Nat Metab* **1**, 1243-1257 (2019).
27. A. J. Chicco, G. C. Sparagna, Role of cardiolipin alterations in mitochondrial dysfunction and disease. *Am J Physiol Cell Physiol* **292**, C33-44 (2007).
28. G. Oemer *et al.*, Phospholipid Acyl Chain Diversity Controls the Tissue-Specific Assembly of Mitochondrial Cardiolipins. *Cell Rep* **30**, 4281-4291 e4284 (2020).
29. J. Li *et al.*, Cardiolipin remodeling by ALCAT1 links oxidative stress and mitochondrial dysfunction to obesity. *Cell Metab* **12**, 154-165 (2010).
30. X. Liu *et al.*, Ablation of ALCAT1 mitigates hypertrophic cardiomyopathy through effects on oxidative stress and mitophagy. *Mol Cell Biol* **32**, 4493-4504 (2012).
31. C. Song *et al.*, Cardiolipin remodeling by ALCAT1 links mitochondrial dysfunction to Parkinson's diseases. *Aging Cell* **18**, e12941 (2019).
32. O. Hahn *et al.*, A nutritional memory effect counteracts benefits of dietary restriction in old mice. *Nat Metab* **1**, 1059-1073 (2019).
33. S. Gumeni, I. P. Trougakos, Cross Talk of Proteostasis and Mitostasis in Cellular Homeodynamics, Ageing, and Disease. *Oxid Med Cell Longev* **2016**, 4587691 (2016).
34. C. Lopez-Otin, M. A. Blasco, L. Partridge, M. Serrano, G. Kroemer, The hallmarks of aging. *Cell* **153**, 1194-1217 (2013).
35. E. Gnaiger, Mitochondrial respiratory states and rates. *MitoFit Preprint Arch* **10.26124/mitofit:190001.v6**, (2019).
36. P. T. Pfluger *et al.*, Simultaneous deletion of ghrelin and its receptor increases motor activity and energy expenditure. *Am J Physiol Gastrointest Liver Physiol* **294**, G610-618 (2008).
37. P. T. Pfluger, D. Herranz, S. Velasco-Miguel, M. Serrano, M. H. Tschop, Sirt1 protects against high-fat diet-induced metabolic damage. *Proc Natl Acad Sci U S A* **105**, 9793-9798 (2008).
38. J. B. Weir, New methods for calculating metabolic rate with special reference to protein metabolism. *J Physiol* **109**, 1-9 (1949).
39. C. Canto, P. M. Garcia-Roves, High-Resolution Respirometry for Mitochondrial Characterization of Ex Vivo Mouse Tissues. *Curr Protoc Mouse Biol* **5**, 135-153 (2015).
40. G. Oemer *et al.*, Molecular structural diversity of mitochondrial cardiolipins. *Proc Natl Acad Sci U S A* **115**, 4158-4163 (2018).
41. T. Pluskal, S. Castillo, A. Villar-Briones, M. Oresic, MZmine 2: modular framework for processing, visualizing, and analyzing mass spectrometry-based molecular profile data. *BMC Bioinformatics* **11**, 395 (2010).
42. C. W. Law, Y. Chen, W. Shi, G. K. Smyth, voom: Precision weights unlock linear model analysis tools for RNA-seq read counts. *Genome Biol* **15**, R29 (2014).
43. S. Falcon, R. Gentleman, Using GOstats to test gene lists for GO term association. *Bioinformatics* **23**, 257-258 (2007).
44. F. Supek, M. Bosnjak, N. Skunca, T. Smuc, REVIGO summarizes and visualizes long lists of gene ontology terms. *PLoS One* **6**, e21800 (2011).

Figure 1.

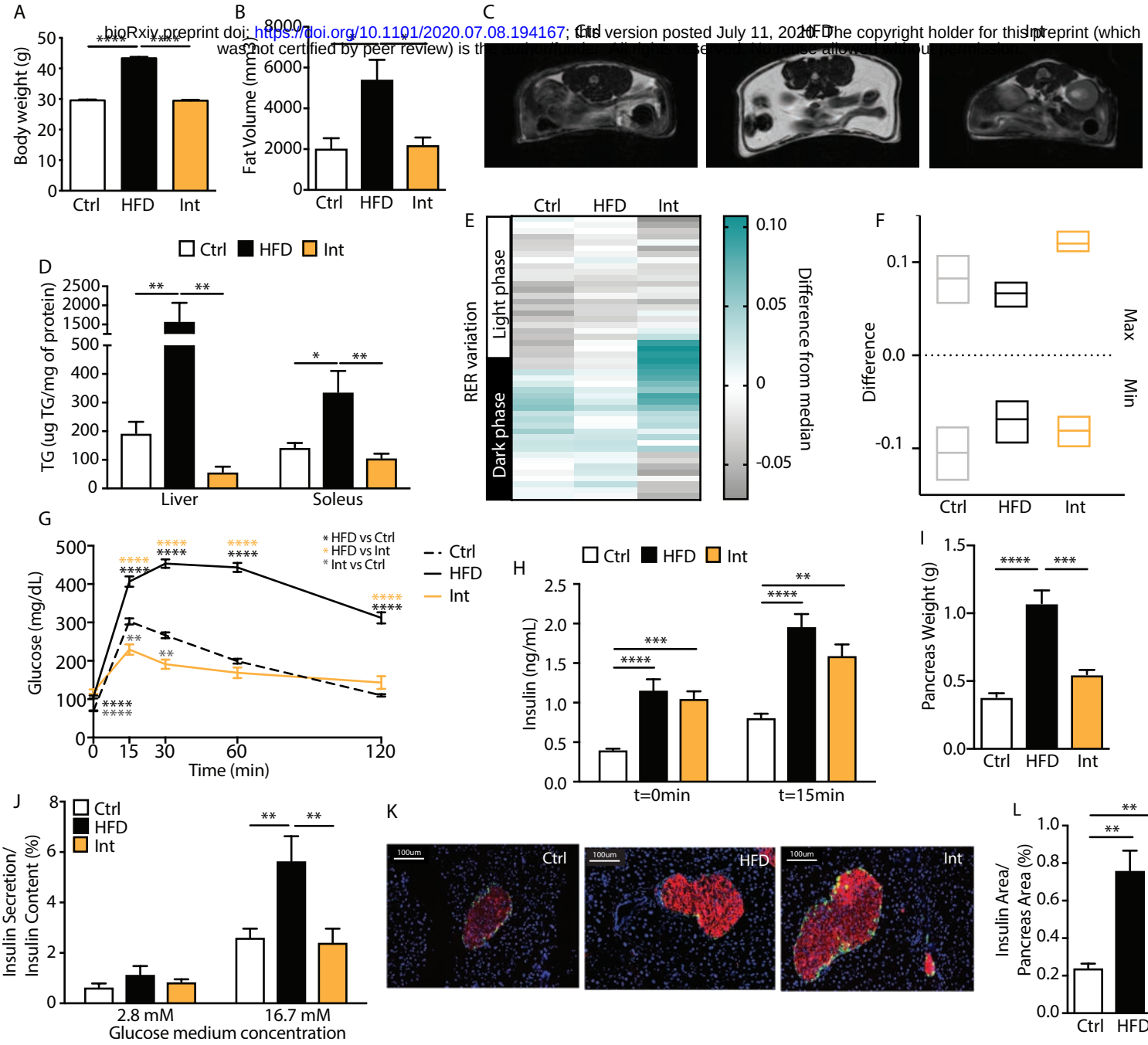

Figure 2.

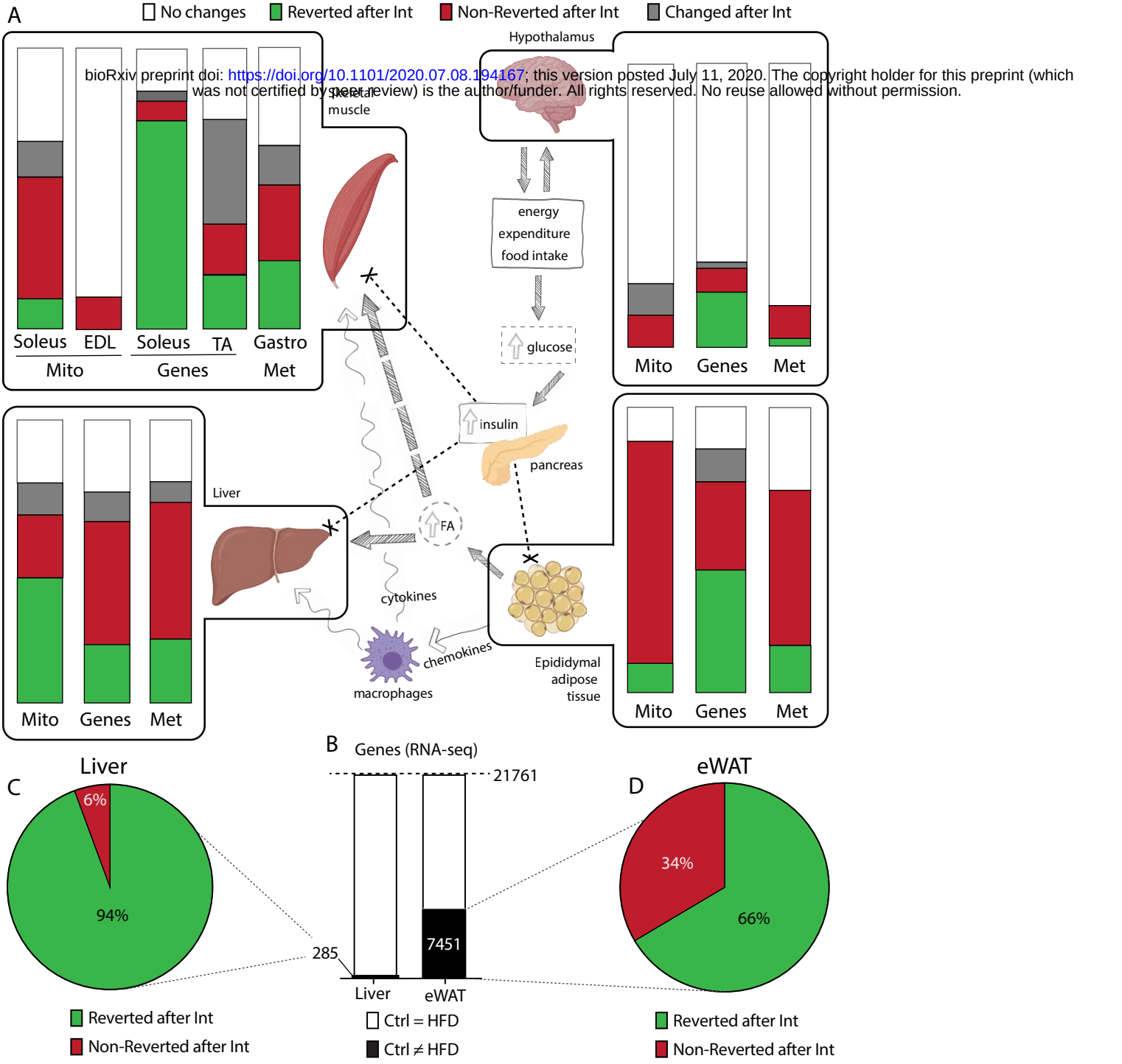

Figure 3.

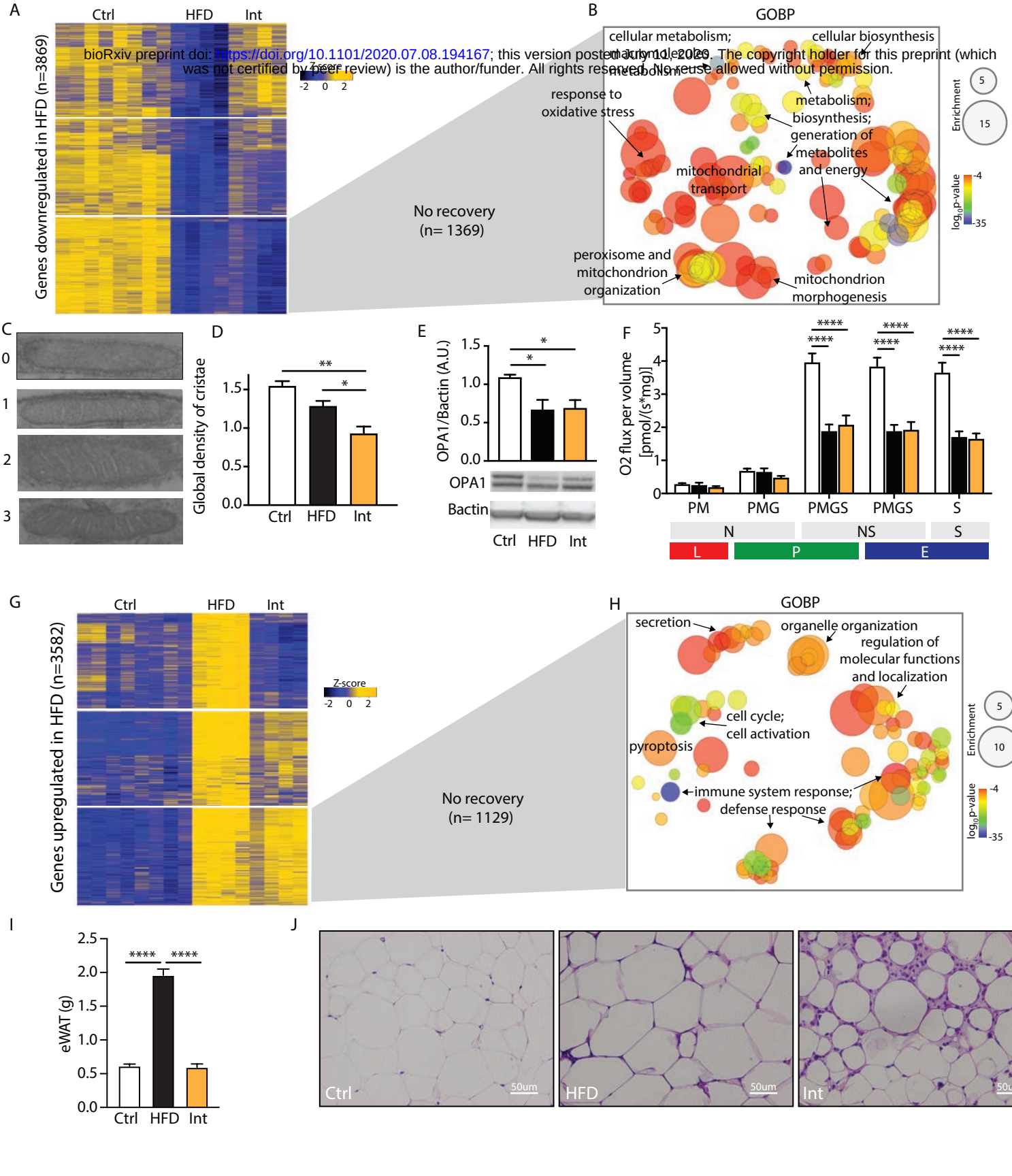

Figure 4.

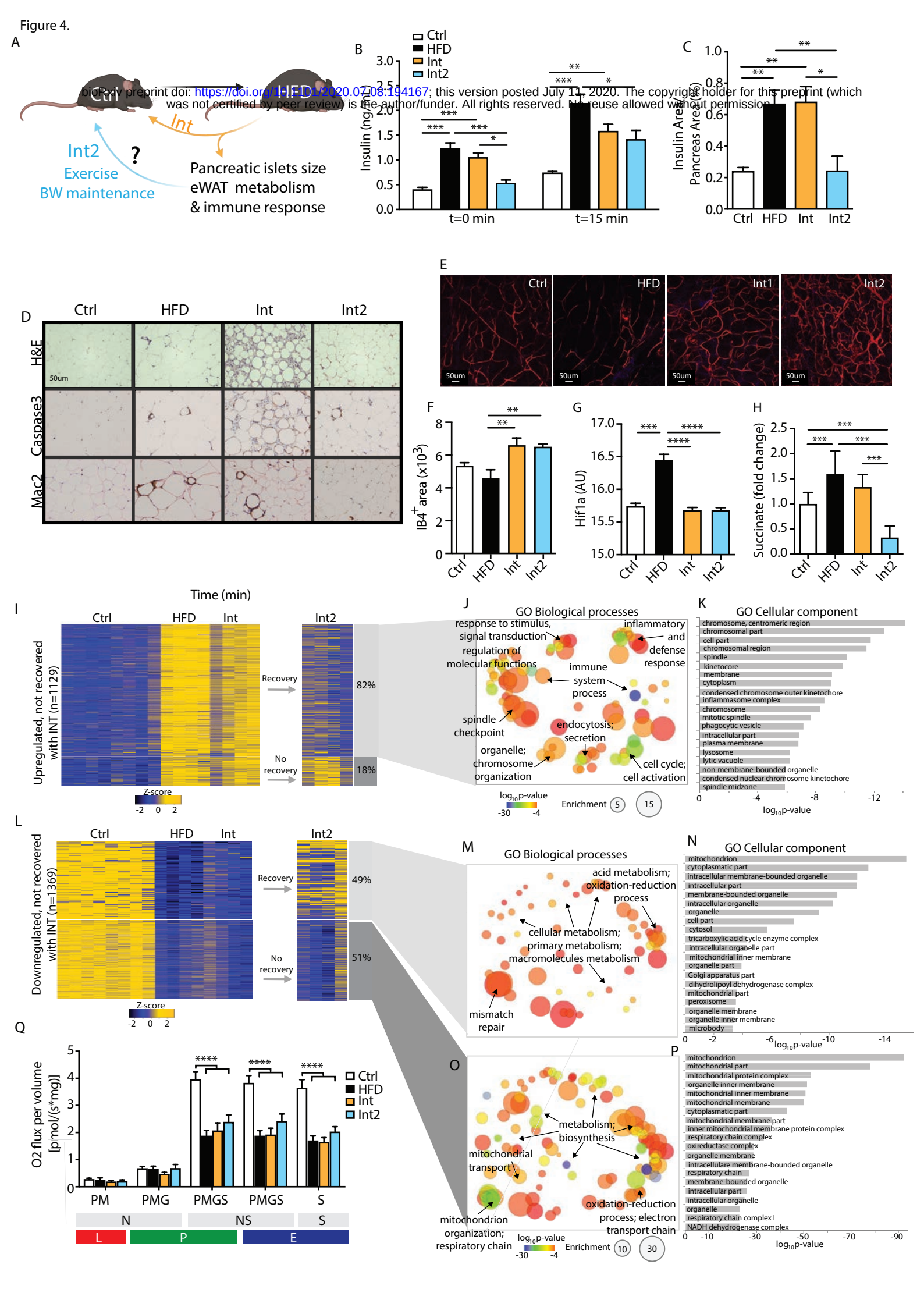

Figure 5.

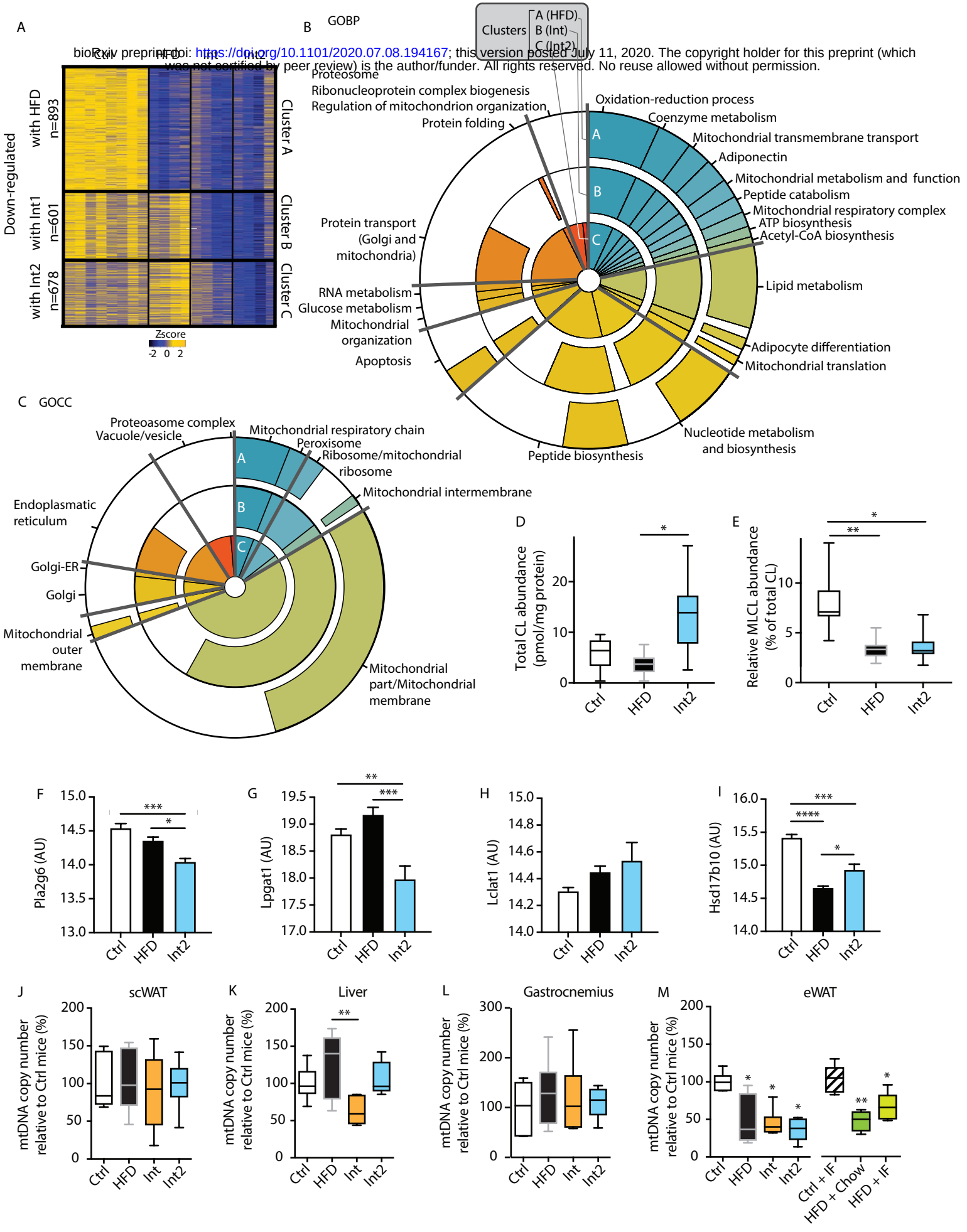

Supplementary information

Supplementary Figure 1. A: Insulin tolerance test in fasted mice (Ctrl n=9; HFD n=6; Int n=6). B: Beta-cell size distribution per pancreas area (Ctrl n=6; HFD n=4; Int n=4). Data represented as mean ± SEM, ANOVA One-way and Post-hoc Tukey, *p<0.05, **p<0.01, ***p<0.001, and ****p<0.0001.

Supplementary Figure 2. A: Detailed representation of Figure 2A uncovering sub-patterns within each group. Different colors indicate the different sub-patterns (in FigureS2A) that correspond to patterns (in Figure 2A). Patterns are grouped in 4 different colors for Figure 2A for simplification. A crossing pattern in Figure S2A indicates no transitivity property, in 3 scenarios: Ctrl vs HFD with no statistical difference, Ctrl vs Int with no statistical difference, but HFD vs Int with a statistical difference (Ctrl≈HFD, Ctrl≈Int, HFD≠Int); when Ctrl≈HFD, Ctrl≠Int, HFD≈Int; and when Ctrl≠HFD, Ctrl≈Int, HFD≈Int.

Supplementary Figure 3. A: Gene ontology cellular components (GOCC) enrichment analysis for the 1369 transcripts downregulated in HFD and Int. B: Percentage of mitochondria within the different mitochondrial cristae frequency categories (Ctrl n=3, HFD n=4, Int n=4). C: Mitochondrial aspect ratio (Ctrl n=3, HFD n=4, Int n=4).

Supplementary Figure 4. A: Body weight evolution in the 4 experimental groups. B: Intraperitoneal glucose tolerance test (IGTT) (Ctrl n=82, HFD n=168, Int n=32, Int2 n=19). C: Quantification for Caspase3- and Mac2-positive cells staining in eWAT for each experimental group (Figure 4D) (Ctrl n=3-4, HFD n=4, Int n=3-4, Int2 n=4-5). D and E: Vegfa (c) and Vegfr (d) normalized eWAT gene expression (Ctrl n=8, HFD n=4, Int n=4, Int2 n=4). Ctrl: control;

HFD: high fat diet-fed; Int: intervention; Int2: second intervention. Data represented as mean ± SEM, ANOVA One-way and Post-hoc Tukey, significant differences with respect to Ctrl *p<0.05, **p<0.01, ***p<0.001, and ****p<0.0001.

Figure S1.

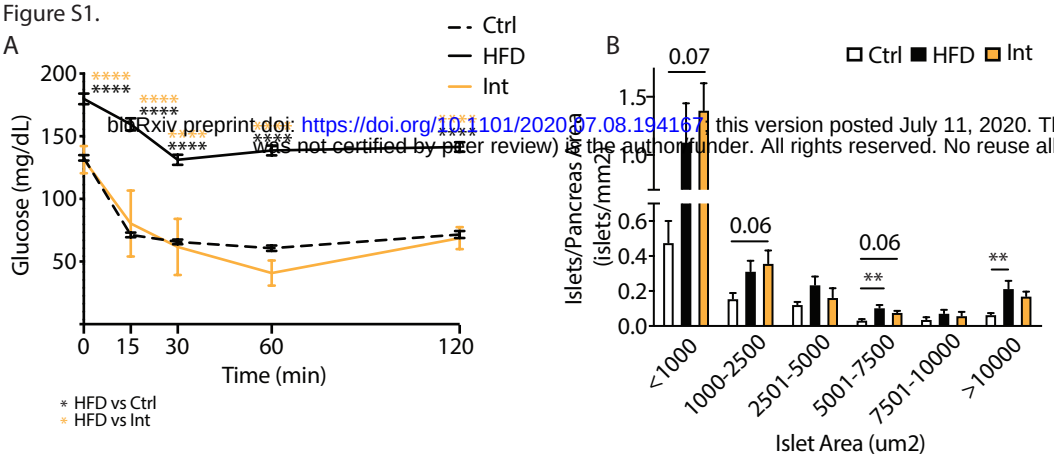

Figure S2.

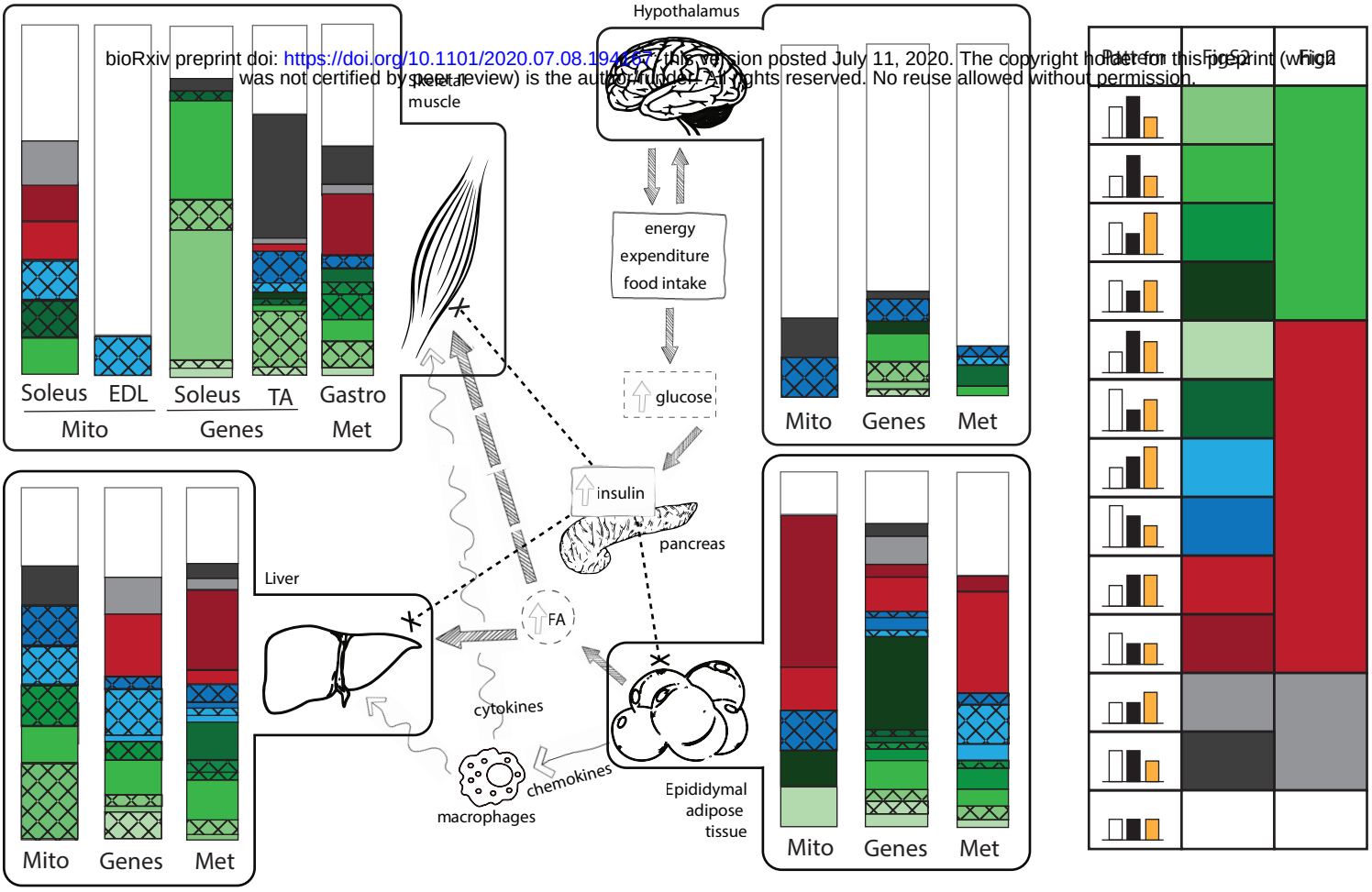

Figure S3.

A

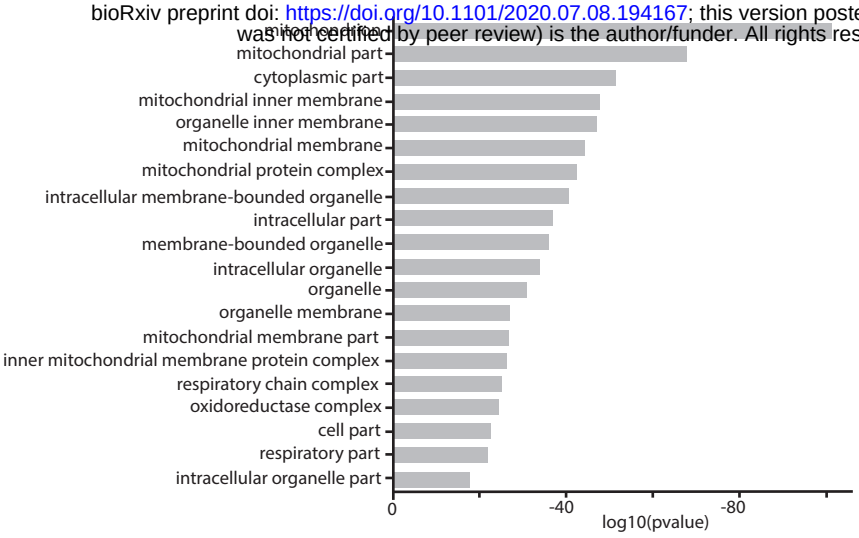

B

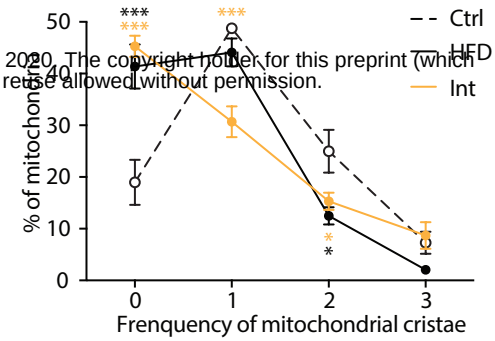

C

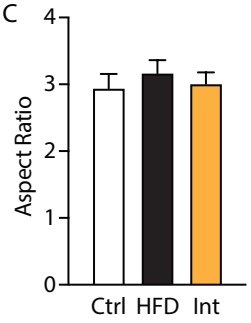

Figure S4.

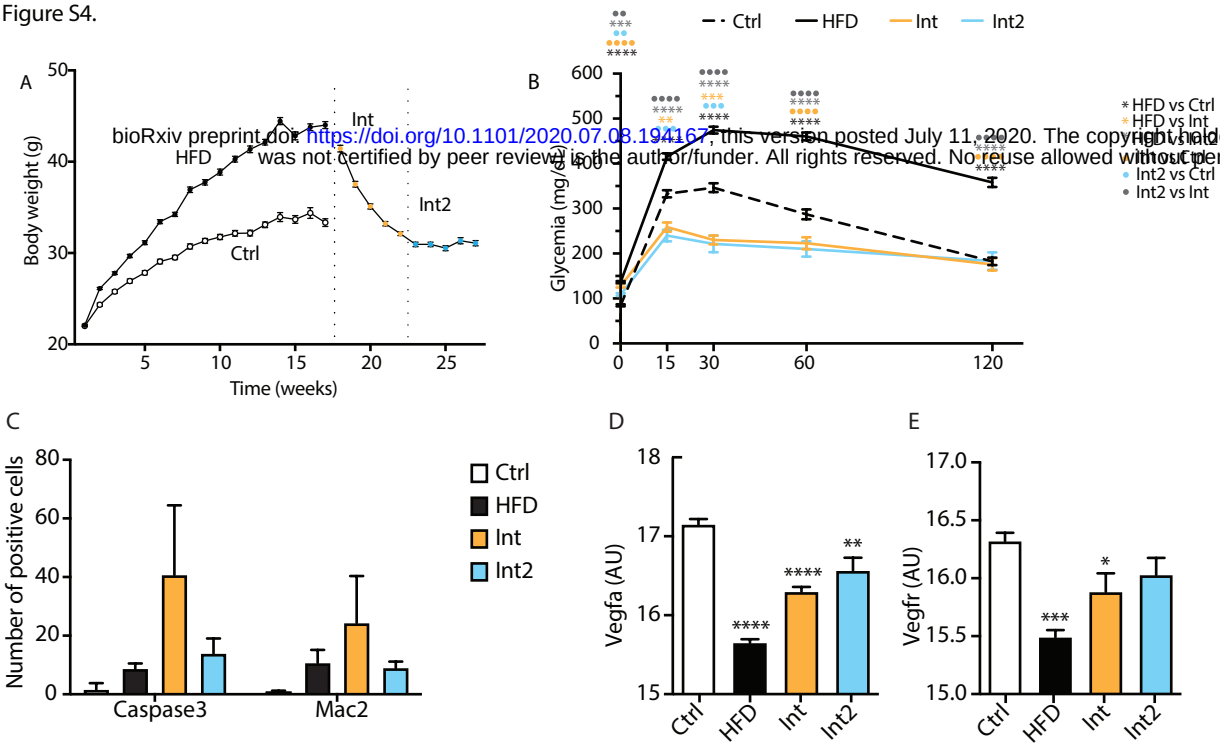

Supplementary Tables 1-7:

http://resources.idibaps.org/paper/obesity-triggers-a-progressive-mitochondrial-deterioration-in-white-adipose-tissue-even-after-a-lifestyle-mediated-phenotypic-reversion

Supplementary Table 1. Gene expression: Gene expression by RT-PCR in the different tissues and experimental groups (corresponding to Figure 2).

https://drive.google.com/open?id=1wArleHoqkSYAnjBa2pRruNz9ytSfG15T

Supplementary Table 2. Gene expression: Gene expression by RNA-seq in the different tissues and experimental groups (corresponding to Figures 2-4).

https://drive.google.com/open?id=1hyla2k2TEFf3zEohlzQRfCnFaCMxGamr

Supplementary Table 3. Metabolomics: Metabolic data for the different tissues and experimental groups (corresponding to Figure 2).

https://drive.google.com/open?id=17hULD46zDsrPFnDdH1sYFfTafW__A7MQ

Supplementary Table 4. Mitochondria function: High-resolution respirometry of the different tissues and experimental groups (corresponding to Figures 2-4).

https://drive.google.com/open?id=1D39FCgM3-npu-CZq_ZLTwNn-h8pN05OZ

Supplementary Table 5. Cardiolipidomics: Cardiolipin anaylsis by liquid chromatography with mass spectrometry for the different experimental groups (Corresponding to Figure 5).

https://drive.google.com/open?id=1rcE8PfkhevjLB5_wRJEeFyznjh4q_1WJ

Supplementary Table 6. Gene ontologies of genes irreversibly decreased with HFD-feeding: Gene ontology biological processes enrichment analysis in the clusters of genes irreversibly decreased with HFD-feeding; from the first intervention and form the second intervention (corresponding to Figure 5).

https://drive.google.com/open?id=1zgEHbjyZvI_ux4VId7zTeAnKXzH_9JHI

Supplementary Table 7. Gene ontologies of genes irreversibly decreased with HFD-feeding: Gene ontology cellular compartments enrichment analysis in the clusters of genes irreversibly decreased with HFD-feeding; from the first intervention and form the second intervention (corresponding to Figure 5).

https://drive.google.com/open?id=1z9VmKXBxGEgiwB3KbOtQ4SyKc_ZF5LMY

Supplementary Table 8. Antibodies, TaqMan probes and mitochondrial substrates, uncoupler and inhibitors (Mitochondrial High-Resolution Respirometry).

	Source	Reference
Antibodies		
Polyclonal Rabbit Anti-Human Glucagon antibody, 1:1000	Dako / Agilent	A0565
Polyclonal Guinea Pig Anti- Insulin antibody, 1:1000	Dako / Agilent	A0564
Donkey Anti-Rabbit IgG (H+L) Antibody, Alexa Fluor 488 Conjugated, 1:500	Life Technologies	A21206
Goat Anti-Guinea Pig IgG Antibody, Alexa Fluor 555 Conjugated, 1:500	Life Technologies	A21435
Mouse Anti-OPA1 Monoclonal Antibody, Unconjugated, Clone 18, 1:1000	BD Biosciences	612606

Rat Anti-Mouse MAC-2 and Gal-3 (Galectin-3) Monoclonal antibody, Unconjugated, Clone m3/38, 1:40000	CEDARLANE	CL8942AP
Cleaved Caspase-3 (Asp175) (5A1E) Rabbit mAb antibody, 1:500	Cell Signaling Technology	9664
Isolectin GS-IB_4 From Griffonia simplicifolia, Alexa Fluor™ 568 Conjugate, 1:2000	Invitrogen	I21412
DAPI		
High-resolution respirometry: substrates, inhibitors and uncoupler		
L-Glutamic acid, sodium salt, C5H8NO4Na	Sigma	G1626
L-Malic acid, C4H6O5	Sigma	M1000
Pyruvic acid sodium salt, C3H3O3Na	Sigma	P2256
Succinate disodium salt, hexahydrate, C4H4O4Na2 x 6 H2O	Sigma	S2378
Cytochrome c	Sigma	C7752
Adenosine 5'diphosphate, C10H15N5O10P2K, potassium salt, contains 1 mol/mol H2O, ADP	Sigma	A5285
Carbonyl cyanide p- (trifluoro-methoxy) phenyl-hydrazone C10H5F3N4O, FCCP	Sigma	C2920
Antimycin A	Sigma	A8674
Rotenone, C23H22O6	Sigma	R8875
Taqman® probes		
acetyl-Coenzyme A carboxylase alpha	Acaca	Mm01304257_m1
adhesion G protein-coupled receptor E1	Adgre1	Mm00802529_m1
agouti related neuropeptide	Agrp	Mm00475829_g1
activating transcription factor 4	Atf4	Mm00515324-m1
activating transcription factor 6	Atf6	Mm01295317-m1
ATP synthase, H+ transporting, mitochondrial F1 complex, alpha subunit 1	Atp5a1	Mm00431960-m1
CART prepropeptide	Cartpt	Mm04210469_m1
catalase	Cat	Mm00437992-m1

chemokine (C-C motif) ligand 2	Ccl2	Mm00441242_m1
CD209e antigen	Cd209e	Mm00459980_m1
CD68 antigen	Cd68	Mm00839636_g1
cell death-inducing DNA fragmentation factor, alpha subunit-like effector A	Cidea	Mm00432554_m1
caseinolytic mitochondrial matrix peptidase chaperone subunit	Clpx	Mm00488586_m1
cytochrome c oxidase subunit IV isoform 1	Cox4i1	Mm01250094-m1
carnitine palmitoyltransferase 1a, liver	Cpt1a	Mm00550438-m1
corticotropin releasing hormone	Crh	Mm01293920_s1
citrate synthase	Cs	Mm00466043-m1
DNA-damage inducible transcript 3	Ddit3	Mm00492097_m1
diacylglycerol O-acyltransferase 2	Dgat2	Mm00499536_m1
dynamin 1-like	Dnm1l	Mm01342903_m1
estrogen related receptor, alpha	Esrra	Mm00433143-m1
fatty acid synthase	Fasn	Mm00662319-m1
fibroblast growth factor 1	Fgf1	Mm00438906_m1
fibroblast growth factor 21	Fgf21	Mm00840165_g1
fission 1 (mitochondrial outer membrane)	Fis1	Mm00481580_m1
forkhead box O1	Foxo1	Mm00490672_m1
GA repeat binding protein, alpha	Gabpa	Mm00484598-m1
glyceraldehyde-3-phosphate dehydrogenase	Gapdh	Mm99999915_g1
glutathione peroxidase 1	Gpx1	Mm00656767-g1
glycogen synthase 1, muscle	Gys1	Mm01962575_s1
glycogen synthase 2	Gys2	Mm00523953_m1
hepatic nuclear factor 4, alpha	Hnf4a	Mm01247716_m1
heat shock protein 5	Hspa5	Mm00517691-m1
heat shock protein 9	Hspa9	Mm00477716_g1
heat shock protein 1 (chaperonin)	Hspd1	Mm00849835_g1
interleukin 10	IL10	Mm00439614_m1
interleukin 1 beta	IL1b	Mm00434228_m1

interleukin 6	IL6	Mm00446190_m1
integrin alpha X	Itgax	Mm00498698_m1
leptin receptor	Lepr	Mm00440181_m1
lon peptidase 1, mitochondrial	Lonp1	Mm01236887_m1
lipoprotein lipase	Lpl	Mm00434764_m1
melanocortin 3 receptor	Mc3r	Mm00434876_s1
melanocortin 4 receptor	Mc4r	Mm00457483_s1
mitofusin 1	Mfn1	Mm00612599_m1
mitofusin 2	Mfn2	Mm00500120_m1
mitochondrially encoded cytochrome c oxidase I	mt-Co1	Mm04225243_g1
mitochondrially encoded cytochrome b	mt-Cytb	Mm04225271_g1
mitochondrially encoded NADH dehydrogenase 3	mt-Nd3	Mm04225292_g1
NADH dehydrogenase (ubiquinone) 1 alpha subcomplex, 9	Ndufa9	Mm00481216-m1
nicotinamide N-methyltransferase	Nnmt	Mm00447994_m1
neuropeptide Y	Npy	Mm00445771_m1
nuclear respiratory factor 1	Nrf1	Mm00447996_m1
optic atrophy 1	Opa1	Mm00453879_m1
phosphoenolpyruvate carboxykinase 1, cytosolic	Pck1	Mm00440636_m1
phosphofructokinase, liver, B-type	Pfkl	Mm00435587_m1
phosphofructokinase, muscle	Pfkm	Mm01309576_m1
pro-opiomelanocortin-alpha	Pomc	Mm00435874_m1
peroxisome proliferator activated receptor alpha	Ppara	Mm00440939_m1
peroxisome proliferator activator receptor delta	Ppard	Mm00803184-m1
peroxisome proliferator activated receptor gamma	Pparg	Mm00440945_m1
peroxisome proliferative activated receptor gamma coactivator 1 alpha	Ppargc1a	Mm01208835-m1
peroxisome proliferative activated recetor gamma coactivator 1 beta	Ppargc1b	Mm01258518_m1
peptidylprolyl isomerase A	Ppia	Mm02342430_g1
stearoyl-Coenzyme A desaturase 1	Scd1	Mm01197142-m1

succinate dehydrogenase complex, subunit A, flavoprotein (Fp)	Sdha	Mm01352366-m1
solute carrier family 2 (facilitated glucose transporter), member 2	Slc2a2	Mm00446224_m1
solute carrier family 2 (facilitated glucose transporter), member 4	Slc2a4	Mm00436615_m1
suppressor of cytokine signalling 3	Socs3	Mm00545913_s1
superoxide dismutase 2, mitochondrial	Sod2	Mm01313000-m1
sterol regulatory element binding transcription factor 1	Srebf1	Mm00550338_m1
transcription factor A, mitochondrial	Tfam	Mm00447485-m1
tumor necrosis factor	Tnf	Mm00443258_m1
ubiquitin-like 5	Ubl5	Mm01151181_m1
uncoupling protein 1 (mitochondrial, proton carrier)	Ucp1	Mm00494069_m1
uncoupling protein 2 (mitochondrial, proton carrier)	Ucp2	Mm00627599_m1
uncoupling protein 3 (mitochondrial, proton carrier)	Ucp3	Mm00494077_m1
ubiquinol cytochrome c reductase core protein 2	Uqcrc2	Mm00445961-m1
X-box binding protein 1 spliced	Xbp1sp	Mm03464496_m1
X-box binding protein 1 total	Xbp1t	Mm00457357_m1